UC Riverside
UC Riverside Previously Published Works

Title

Magnetically Induced Anisotropic Interaction in Colloidal Assembly.

Permalink

https://escholarship.org/uc/item/2j2295qp

Journal

Precision Chemistry, 1(5)

Authors

Fan, Qingsong
Li, Zhiwei
Wu, Chaolumen
et al.

Publication Date

2023-07-24

DOI

10.1021/prechem.3c00012

Peer reviewed

Magnetically Induced Anisotropic Interaction in Colloidal Assembly

Qingsong Fan, Zhiwei Li, Chaolumen Wu, and Yadong Yin*

Cite This: *Precis. Chem.* 2023, 1, 272−298

Read Online

ACCESS | Metrics & More | Article Recommendations

ABSTRACT: The wide accessibility to nanostructures with high uniformity and controllable sizes and morphologies provides great opportunities for creating complex superstructures with unique functionalities. Employing anisotropic nanostructures as the building blocks significantly enriches the superstructural phases, while their orientational control for obtaining long-range orders has remained a significant challenge. One solution is to introduce magnetic components into the anisotropic nanostructures to enable precise control of their orientations and positions in the superstructures by manipulating magnetic interactions. Recognizing the importance of magnetic anisotropy in colloidal assembly, we provide here an overview of magnetic field-guided self-assembly of magnetic nanoparticles with typical anisotropic shapes, including rods, cubes, plates, and peanuts. The Review starts with discussing the magnetic energy of nanoparticles, appreciating the vital roles of magneto-crystalline and shape anisotropies in determining the easy magnetization direction of the anisotropic nanostructures. It then introduces superstructures assembled from various magnetic building blocks and summarizes their unique properties and intriguing applications. It concludes with a discussion of remaining challenges and an outlook of future research opportunities that the magnetic assembly strategy may offer for colloidal assembly.

KEYWORDS: *colloidal self-assembly, magnetic field-guided self-assembly, magnetic nanoparticles, magnetic anisotropy, superstructures, magneto-crystalline anisotropy, shape anisotropy*
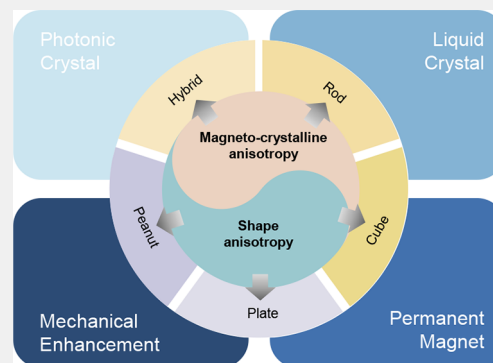
1. INTRODUCTION

Nanostructured materials have seen rapid development in the past few decades because of their promising technological applications. Compared with individual nanoparticles or random aggregates, ordered arrangements of nanoparticles often lead to extraordinary collective properties that can delicately exploit the synergy between adjacent building blocks, inducing pronounced enhancement in optical,[1−5] plasmonic,[4,6−9] catalytic,[10,11] electronic,[12] magnetic,[13,14] and mechanical properties.[15−17] However, acquiring such ordered arrangements is a nontrivial task. One of the most promising strategies is colloidal self-assembly,[18,19] the spontaneous organization of colloidal nanoparticles due to direct specific interactions typically associated with thermodynamic equilibrium.[20] Various self-assembly methods have been reported with great success for spherical nanoparticles.[19,21−25] However, when nanoparticles with nonspherical shapes are used as the building blocks, most self-assembly methods result in unsatisfactory long-range packings due to a lack of efficient orientational control of the nanoparticles.

Anisotropic nanoparticles with magnetic properties may be assembled with orientation control in external magnetic fields. It has been known for over 2000 years that the magnetized ladle can be used to indicate directions.[26] When magnetic nanoparticles are subjected to an external magnetic field, the induced magnetic dipoles interact with the magnetic field and get aligned parallel to the field line to reduce their magnetic energy. This classic interaction allows precise orientational control of individual nanoparticles. Besides, the magnetic field-assisted self-assembly has many other advantages,[27] including (1) highly directional magnetic dipole−dipole interactions among nanoparticles,[28] which enables flexible experimental designs; (2) strong, reversible, and remote manipulation of magnetic interactions,[29,30] rapid assembly of colloidal particles of different shapes; (3) widely accessible magnetic fields with programmable strengths and spatial distributions for fine control over the assembly of colloidal particles.[31]
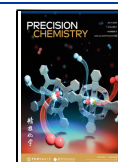
To better design the assembled superstructures using magnetic nonspherical nanoparticles, it is imperative to understand the role of magnetic anisotropy in the assembly process. Magnetic anisotropy refers to the phenomenon that the energy of a magnetic body depends on the direction of the magnetization with respect to its shape or crystal axes.[32]

Magnetic anisotropy determines the orientation of individual nanoparticles relative to the magnetic field and is dependent on various factors, such as crystal domain size, crystal phase, crystal microstructure, particle shape, and surface stabilization. A general introduction to these factors is included in Section 2, with more detailed discussions given in section 4 for nanostructures of different shapes.

This Review summarizes the various superstructures assembled from magnetic nanoparticles with anisotropic morphologies and emphasizes the importance of magnetic anisotropy in assembling nonspherical nanoparticles. It mainly focuses on but is not limited to the ordered superstructures assembled from nanostructures of different shapes. The magnetic energy and interactions are introduced in Section 2, where some basic concepts related to magnetic anisotropy are briefly introduced. The assembled superstructures are then described in Sections 3 and 4, which start with isotropic magnetic nanoparticles as building blocks and extend the discussion to magnetic nanoparticles with anisotropic morphologies. Finally, the applications of the assembled superstructures in photonic crystals, liquid crystals, permanent magnets, and mechanical enhancement materials are summarized in Section 5. We conclude this Review with existing challenges in the magnetic field-guided assembly of anisotropic nanoparticles and provide perspectives on the future development of this promising research field.

2. MAGNETIC ENERGY AND INTERACTIONS

2.1. Magnetic Energy of a Single Nanoparticle

The magnetic properties of a particle can be described by the anisotropic Heisenberg model. Based on this model, the total energy of a magnetic material is the sum of several terms:[33]

$$E_{total} = E_{crystalline} + E_{shape} + E_{surface} + E_{elastic} + E_{Zeeman} + E_{exchange} \tag{1}$$

where $E_{crystalline}$ is the magneto-crystalline energy, E_{shape} is the shape anisotropy energy, $E_{surface}$ is the surface anisotropy energy, $E_{elastic}$ is the magnetoelastic energy, E_{Zeeman} is the Zeeman energy arising from the interaction between the magnetic dipoles of the material and the external magnetic field, and $E_{exchange}$ is the exchange energy. Magnetic anisotropy is used to describe the dependence of the internal energy on the direction of spontaneous magnetization. Consequently, easy and hard directions of magnetization develop, corresponding to the material's minimal and maximum total energy, respectively. In eq 1, the first four terms contribute to the magnetic anisotropy of a particle.

2.1.1. Magneto-crystalline Energy. Due to the ordered arrangement of neighboring atoms in a single crystal domain of a magnetic material, the strong spin−orbital coupling results in magnetic dipole enhancement in certain crystallographic axes, which is called directions of easy magnetization; the directions along which it is the most difficult to magnetize the crystal are called the hard directions.[34] This is the major cause of magnetic anisotropy, especially in bulk magnetic materials.

Magneto-crystalline energy can show various symmetries, with uniaxial and cubic forms being the two major cases.[35] The uniaxial anisotropy is associated with the hexagonal, tetragonal, and rhombohedral crystal symmetry. If only these first two terms are considered, the magneto-crystalline energy of single-domain crystals with the uniaxial anisotropy depends on the

polar angle θ but not on the azimuthal angle φ of the magnetization direction, and it can be calculated using[32]

$$E_{crystalline}^{uniaxial} = V(K_{u1}\sin^2\theta + K_{u2}\sin^4\theta) + ... \tag{2}$$

where K_{un} is the nth uniaxial magneto-crystalline anisotropy constant and V is the crystal volume. The first anisotropy constant K_{u1} is often the leading consideration: when $K_{u1} > 0$, energy minima are at $\theta = 0°$ and $\theta = 180°$, which has a preferential magnetization direction along the c-axis of the crystal (Figure 1A); when $K_{u1} < 0$, the energy is minimized at θ
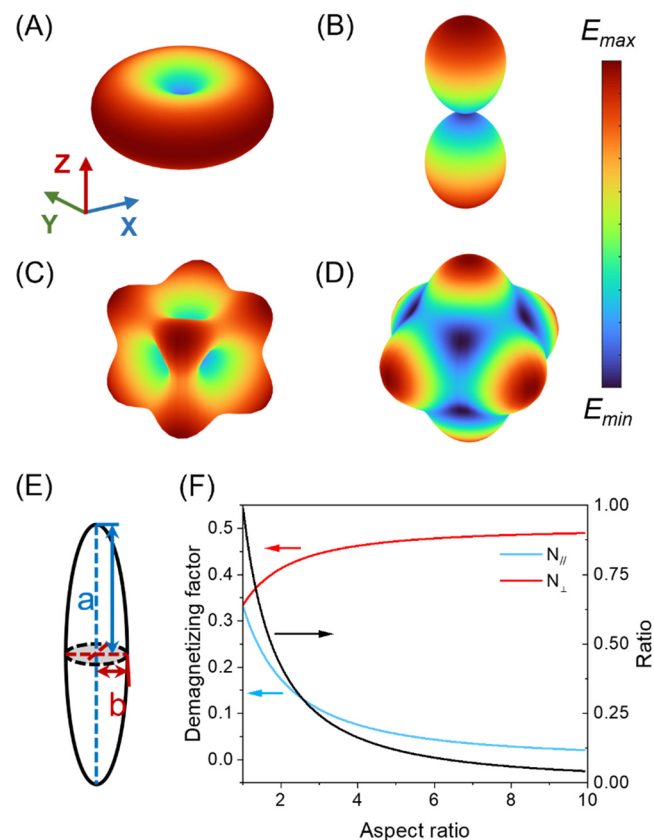
Figure 1. (A, B) Uniaxial magneto-crystalline anisotropy energy surface for (A) $K_{u1} > 0$ and (B) $K_{u1} < 0$. (C, D) Cubic magneto-crystalline anisotropy energy surface for (C) $K_{c1} > 0$ and (D) $K_{c1} < 0$. (E) Schematic representation of an ellipsoid. (F) Demagnetizing factor and the ratio (parallel/perpendicular) for an ellipsoid as a function of aspect ratio.

$= 90°$, which has a preferential magnetization direction in the plane perpendicular to the c-axis (Figure 1B). For most magnetic materials with uniaxial crystal symmetry, the experimentally determined K_{u1} values are usually positive, and the c-axis of its crystal lattice is therefore the easy magnetization axis in terms of magneto-crystalline energy.[36]

In crystals with cubic symmetry, the magneto-crystalline energy is given by[32]

$$E_{crystalline}^{cubic} = V[K_{c1}(\alpha^2\beta^2 + \beta^2\gamma^2 + \alpha^2\gamma^2) + K_{c2}\alpha^2\beta^2\gamma^2 + ...] \tag{3}$$

where K_{cn} is the nth cubic magneto-crystalline anisotropy constant and α, β, γ are the cosines of the angles between the magnetization and the axes X, Y, Z parallel to the 4-fold axes, respectively. In the cubic symmetry system, if the second term

Table 1. Properties of Some Common Magnetic Materials

	name	crystal system	magneto-crystal anisotropy (RT)	chemical stability
metal	Fe	cubic[37−40]	$K_1 = 4.8 \times 10^4$ J m^{-3} [41]	easy to be oxidized
	Ni	cubic[42−44]	$K_1 = -4.8 \times 10^3$ J m^{-3} [41]	easy to be oxidized
		hexagonal [45]		
	Co	hexagonal[46−49]	$K_1 = 5.3 \times 10^5$ J m^{-3} [41]	easy to be oxidized
metal alloy	FePt	tetragonal/cubic[50−52]	$K_1 = 6.6 \times 10^6$ J m^{-3} [41]	more stable than Fe
	FeCo	cubic[53,54]		easy to be oxidized
metal oxide	α-Fe$_2$O$_3$	trigonal[55,56]	$K_1 = -7 \times 10^3$ J m^{-3} [36]	stable
	γ- Fe$_2$O$_3$	cubic[57,58]	$K_1 = -4.6 \times 10^3$ J m^{-3} [41]	stable
	Fe$_3$O$_4$	cubic[59−61]	$K_1 = -1.1 \times 10^4$ J m^{-3} [41]	less stable than Fe$_2$O$_3$
	MnFe$_2$O$_4$	cubic[62,63]	$K_1 = -2.8 \times 10^3$ J m^{-3} [41]	stable
	CoFe$_2$O$_4$	cubic[62−64]	$K_1 = 2.7 \times 10^5$ J m^{-3} [41]	stable

and higher order terms can be neglected, the easy axes are the [100] axes for $K_{c1} > 0$ (Figure 1C, i.e., Fe and CoFe$_2$O$_4$) and the [111] directions for $K_{c1} < 0$ (Figure 1D, i.e., Ni, Fe$_3$O$_4$ and most ferrites). More complex situations arise when both K_{c1} and K_{c2} are taken into consideration. It should be noted that in certain cases where a rough estimation is sufficient, materials with cubic anisotropy are often approximated as having uniaxial anisotropy for computational simplicity. Table 1 summarizes the crystal system and magneto-crystalline anisotropy (K_1) of some common magnetic materials. Readers interested in more details are referred to the related literature.[32]

2.1.2. Shape Anisotropy Energy. Shape anisotropy energy, also known as magnetostatic self-energy or demagnetizing energy, is the potential energy of a particle in the field created by its own magnetization.[65] The general equation of shape anisotropy energy is

$$E_{shape} = -\frac{1}{2}\mu_0 \int_V \boldsymbol{M} \cdot \boldsymbol{H}_d \, \mathrm{d}r^3 \tag{4}$$

where $\boldsymbol{M}$ is the local magnetization of the particle, and $\boldsymbol{H}_d$ is the demagnetization field. The demagnetization field is created as long as there are discontinuities on the surface of the sample of the normal component of the magnetization. For a nonspherical particle, its long axis's demagnetization factor is smaller than its short axis, making it easier to magnetize along its long direction, because the induced magnetic poles at the surface are further apart in the long direction.[66]

For a magnetic particle with ellipsoidal shape, if we define the magnetization and demagnetization factors relative to the x, y, and z directions of the crystal as M_x, M_y, M_z and N_x, N_y, N_z, respectively, the shape anisotropy energy of a uniform magnetized ellipsoid can be expressed as[67]

$$E_{shape} = \frac{1}{2}\mu_0 \left(N_x M_x{}^2 + N_y M_y{}^2 + N_z M_z{}^2\right) \tag{5}$$

where the demagnetization factors satisfy the normalization relation $N_x + N_y + N_z = 1$.

If the z-axis is the major axis of this ellipsoid (Figure 1E), this energy then becomes

$$E_{shape} = \frac{1}{2}\mu_0 V M_s{}^2 \left(N_z\cos^2\theta + N_x\sin^2\theta\right) \tag{6}$$

where M_s is the saturation magnetization, N_z and N_x ($N_z < N_x = N_y$) are the demagnetization factors along the polar and the equatorial axes, and θ is defined as the angle between the direction of magnetization and the long axis of the particle. An elongated nanocrystal in the z direction minimizes its shape

energy by aligning the magnetization direction with the long axis of the particle, while its shape energy is highest for a magnetization direction perpendicular to the long axis. Obviously, a uniformly magnetized single-domain spherical particle has no shape anisotropy, and the demagnetizing factors are isotropic in all directions ($N_x = N_y = N_z = 1/3$). The relationship between the demagnetization factor and the aspect ratio of an ellipsoid is shown in Figure 1F.

2.1.3. Surface Anisotropy Energy. Surface anisotropy energy comes from the atoms located at the material's surface since they have incomplete coordination spheres and a broken symmetry compared to the core atoms. Such a decrease in the crystalline symmetry at the surface induces a different orientation of the surface spins with respect to the magnetization direction.[68] This energy is negligible for bulk materials with small specific surface areas compared to other energies. However, in some cases, shrinking magnetic materials to nano- or microscale induces a comparable or even dominant contribution to magnetic anisotropy. The surface anisotropy energy can be expressed as[68]

$$E_{surface} = K_{surface} \int_S \cos^2\theta \, \mathrm{d}S \tag{7}$$

where $K_{surface}$ is the surface anisotropy density constant, θ is the angle between the magnetization and the normal to the surface. The sign of the surface energy depends on the nature of the crystal lattice and the surface orientation.

For magnetic nanocrystals synthesized through bottom-up approaches (i.e., colloidal synthesis), the coordination sphere of the surface atoms is partially recovered due to the presence of capping ligands on the surface of the nanocrystals.[69] Therefore, the broken symmetry and the surface anisotropy effect are reduced; hence, the surface spins are more easily aligned with the magnetization direction. Therefore, the surface effects of the colloidal nanocrystals strongly depend on the synthesis process and the crystal quality.

Although various mechanisms are proposed for the surface-spin misalignment, such as the magnetic dead layer, surface spin canting, and noncollinear surface spins,[70,71] the possible mechanisms are still debatable. Therefore, this Review does not include extensive discussion on the contribution of these mechanisms to the basic understanding of the magnetic behavior of anisotropic nanoparticles.

2.1.4. Magnetoelastic Energy. Magnetoelastic energy is related to the magnetostriction that occurs in magnetic materials. When the crystals are magnetized, the interatomic distance can vary with the intensity and the orientation of magnetization.[72,73] This effect also accounts for the hysteresis

loop distortion of a magnetic material under mechanical stress.[74,75] However, giving a general formulation for describing the magnetoelastic energy is challenging since this effect is highly dependent on the sample and the elaboration method.

2.1.5. Zeeman Energy. Zeeman energy is the potential energy of a magnetic material in an external magnetic field. It arises from the interaction between the magnetic dipoles of the material and the applied magnetic field and can be described as[76]

$$E_{Zeeman} = -\mu_0 \int_V \boldsymbol{M} \cdot \boldsymbol{H}_{ext} \, \mathrm{d}V \tag{8}$$

where $\boldsymbol{H}_{ext}$ is the external field and $\boldsymbol{M}$ is the local magnetization of the particle. Zeeman energy is minimum when $\boldsymbol{M}$ and $\boldsymbol{H}_{ext}$ are parallel, while this energy is maximum when they are antiparallel. The minimization of Zeeman energy is the cause of the rotation of magnetic materials in the external magnetic field at all length scales.

2.1.6. Exchange Energy. The phenomenon whereby an individual atomic magnetic moment attempts to align all other atomic magnetic moments with itself within a material is known as the exchange interaction.[77,78] Typically, this interaction is considered only effective in short-range and does not contribute to the magnetic anisotropy because it only tends to produce large magnetic domains and is not related to the direction of the domains. However, the long-range indirect exchange interactions through Ruderman–Kittel–Kasuya–Yosida (RKKY) coupling may occur in some systems.[79,80] Since its contribution to the overall magnetic anisotropy is less significant than the others, a more detailed discussion on this point is omitted from this Review.

It is also worth noting that in nanoparticles consisting of a ferromagnetic (FM) core and an antiferromagnetic (AFM) shell, exchange bias resulting from the exchange anisotropy can be created at the interface between the FM and AFM materials. Readers interested in this phenomenon are encouraged to explore relevant references for further information.[81–83]

Based on the above discussion, the interplay of magneto-crystalline, shape anisotropy, and surface anisotropy determines the final easy magnetization direction of a nanoparticle. More explicitly, the magnetic anisotropy of a nanoparticle is influenced by its crystal domain size, crystal phase, crystal microstructure (mono- or polycrystallinity), particle shape, and surface stabilization. These various factors create nanoparticles with a variety of different magnetic anisotropies and thereby enrich the assembled superstructures.

2.2. Magnetic Interaction among Adjacent Nanoparticles

When magnetic colloidal nanoparticles are employed as building blocks to obtain more complex secondary structures, the magnetic interactions among these particles significantly affect the final superstructures. Two methods are commonly used to calculate this interparticle interaction: (1) the dipole approximation method and (2) the finite element method.

2.2.1. Dipole Approximation Method. In the dipole approximation method, each particle is considered to possess an overall effective dipole located at its geometry center when calculating the magnetic forces among nanoparticles. Because of its simplicity and effectiveness, this method is widely applied to analyze the interaction between particles with different shapes (i.e., sphere,[84–86] cube,[87–90] rod,[91] etc.) and sizes (ranging from nanoscale to microscale).

The magnetic dipole–dipole coupling energy of two dipoles can be given by[84,92]

$$E_{dd,12} = -\frac{\mu_f}{4\pi}\left(3\frac{(\boldsymbol{m}_1 \cdot \boldsymbol{r}_{12})(\boldsymbol{m}_2 \cdot \boldsymbol{r}_{12})}{r_{12}{}^5} - \frac{\boldsymbol{m}_1 \cdot \boldsymbol{m}_2}{r_{12}{}^3}\right) \tag{9}$$

where $\boldsymbol{m}_1$ and $\boldsymbol{m}_2$ are the dipole moments of the first and second particles, respectively; $\boldsymbol{r}_{12}$ is the displacement vector between them.

This dipole–dipole coupling energy has two features. First, it is a long-range interaction, and the coupling energy from all other particles should be considered when multiple particles are present. Second, this energy shows an angular-dependent feature influenced by the relative orientation of two dipoles and the angle between the dipole and the displacement vector.

2.2.2. Finite Element Method. The dipole approximation method does not take shapes into consideration and may result in errors, especially in the following situations: the particles of complex shapes have low symmetry, and their magnetic dipoles do not overlap with their geometry centers, or the separation between particles is so small that the local effects are important and cannot be ignored. In these cases, the finite element method can provide a more accurate force calculation and analysis.

In the finite element method, a particle with complex geometry is divided into many subdomains, and each small subdomain is regarded as a magnetic dipole that can interact with other dipoles. The force is obtained by integrating over the whole volume of the particle. This method has been applied to analyze the magnetic interactions between anisotropic nanoparticles.[2,93,94]

3. ISOTROPIC MAGNETIC NANOPARTICLES

The total magnetic energy of isotropic magnetic nanoparticles does not change with the orientation of their magnetic dipoles relative to their shapes. One typical example is the spherical magnetic clusters composed of crystal domains with random orientation.[95–101] The random orientation of crystal domains and the spherical symmetry eliminates the magnetic anisotropy in terms of magneto-crystalline and shape anisotropy.

Due to the spherical symmetry, the dipole approximation method is sufficient to describe the magnetic interaction. One special condition of particular interest is the coupling energy of two identical particles with coaligned moments which are induced by a uniform applied field ($\boldsymbol{m}_1 = \boldsymbol{m}_2 = \boldsymbol{m}$). Thus, eq 9 can be simplified as

$$E_{dd,12} = -\frac{\mu_f}{4\pi}\frac{m^2}{r_{12}{}^3}(3\cos^2\theta - 1) \tag{10}$$

where θ is the angle between the magnetic dipole and the displacement vector. This energy is minimum when $\theta = 0°$ or $180°$ and maximum when $\theta = 90°$ or $270°$. The same conclusion can be drawn by analyzing the magnetic force between these two dipoles, which can be derived from the gradient of the coupling energy:

$$\begin{aligned} \boldsymbol{F}_{dd,12} &= -\nabla E_{dd,12} \\ &= -\frac{3\mu_f}{4\pi}\frac{m^2}{r_{12}{}^4}((3\cos^2\theta - 1)\hat{\boldsymbol{r}} + \sin(2\theta)\hat{\boldsymbol{\theta}}) \end{aligned} \tag{11}$$

where $\hat{\boldsymbol{r}}$ and $\hat{\boldsymbol{\theta}}$ are the unit vectors parallel and perpendicular to the displacement vector, respectively. In Figure 2, the plane is
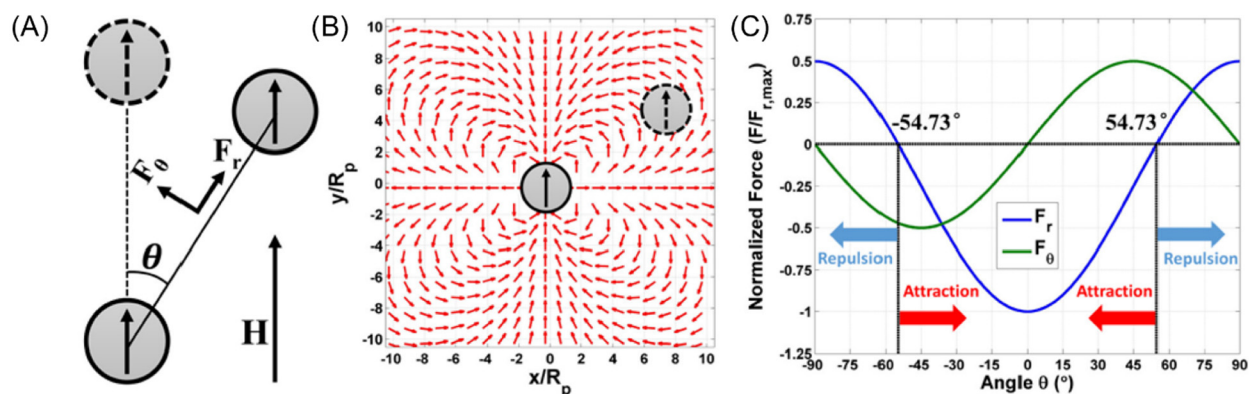
Figure 2. Dipole−dipole interaction between two magnetic nanospheres. (A) Geometry showing the relative position of interacting dipoles and direction of applied field. (B) Normalized dipole−dipole force field. (C) Normalized dipole−dipole force components as a function of relative angular position θ as shown in (A). Reproduced from ref 107. Copyright 2015 American Chemical Society.

divided into 4 regions, with 2 attractive regions and 2 repulsive regions. This directional magnetic interaction favors the formation of chain structures within which the magnetic dipoles are arranged in a head-to-tail manner.[102−106]

4. ANISOTROPIC MAGNETIC NANOPARTICLES

The development of nanotechnology in the past few decades has driven the synthesis of a variety of anisotropic magnetic particles with uniform sizes, such as rods, cubes, plates, and peanuts.[108−112] Here, we examine the easy magnetization directions for anisotropically shaped nanoparticles prepared from different synthesis methods and their corresponding assembled superstructures.

It is worth mentioning that to obtain ordered superstructures by the colloidal assembly, the magnetic particles as building blocks need to have a remanence as low as possible. A large remanence of the magnetic particles will cause the following issues: (1) The strong dipole−dipole interaction among particles causes severe aggregation even without applying the external magnetic field, leading to many misalignments and defects during the subsequent assembly. (2) In many cases, a reversible switch between the assembled and disassembled states is desired, which is not achievable using building blocks with a large remanence unless a demagnetization process is provided.

The remanence of a magnetic particle largely depends on the material and crystal domain size. When the crystal domain is below a certain value, thermal energy (k_BT) is high enough to freely rotate the magnetic dipole in the particle, resulting in zero remanence. A nanoparticle with zero remanence is known to be in its superparamagnetic state,[113] and the critical domain size (D_{sp}) can be calculated from the correlation between the thermal energy (k_BT) and the magneto-crystalline anisotropy constant (K_1):[110]

$$D_{sp} = \left(\frac{48 k_\mathrm{B} T}{K_1} \right)^{1/3}$$

(12)

This equation shows that materials with a low magneto-crystalline anisotropy constant have a larger critical domain size. It explains why the magnetic nanoparticles for colloidal assembly are usually those materials with low magneto-crystalline anisotropy constant, such as Fe, Ni, and Fe_3O_4, instead of $SmCo_5$ and NdFeB particles.

4.1. Nanorods

4.1.1. Easy Magnetization Direction of Nanorods.
Rods have uniaxial symmetry, with the combination of shape anisotropy and magneto-crystalline anisotropy determining their overall magnetic anisotropy. For shape anisotropy energy, the easy axis is parallel to its long axis due to the large difference between the demagnetizing factors in the polar and the equatorial axes, i.e., for a rod with an aspect ratio of 5, the demagnetizing factor ratio = 0.12. When the magneto-crystalline easy axis coincides with its shape anisotropy easy axis or the effect of magneto-crystalline anisotropy is not comparable with the shape anisotropy, the overall effective easy direction of magnetization is then along the long axis of the nanorods. For example, Wang et al. obtained Fe_3O_4 nanorods with diameters of 20−25 nm and lengths up to 200−300 nm from ferric chloride and diamine hydrate using hydrothermal reaction with polyethylene glycol as a surfactant (Figure 3A).[114] The as-synthesized rods are single crystalline with the [110] direction as their growth direction, as shown in Figure 3B. This direction matches one intermediate easy magnetization axis of the cubic structure of magnetite. Dumestre et al. synthesized monodisperse single crystalline Co nanorods by the decomposition of organometal of Co (Figure 3C).[48] The size of Co nanorods can be tuned by changing the ligands and concentrations. The high-resolution transmission electron microscopy (HRTEM) measurement confirmed their hexagonal close-packed crystal structure with the *c*-axis ([0001]) oriented along the growth direction (Figure 3D). The cooperation of magneto-crystalline anisotropy and shape anisotropy easy axis makes the long axis of these nanorods the overall easy magnetization direction.

However, a magnetic nanowire with an easy magnetization direction perpendicular to its long axis has also been reported. Kim et al. synthesized vertically aligned α-Fe_2O_3 nanowire arrays on a substrate via the thermal oxidation of Fe foil.[115] The single crystalline nanowires have diameters of 100−300 nm and a length of ~15 μm with a rhombohedral crystal structure and [11$\bar{2}$0] as their growth direction (Figure 3E and F). Magnetic hysteresis loop measurement suggests that the short axis is the easy magnetization direction of these nanowires. In this case, the short axis ([0001] direction) is the easy axis of magneto-crystalline anisotropy, which is much stronger than the shape anisotropy and thus determines the overall easy magnetization direction.
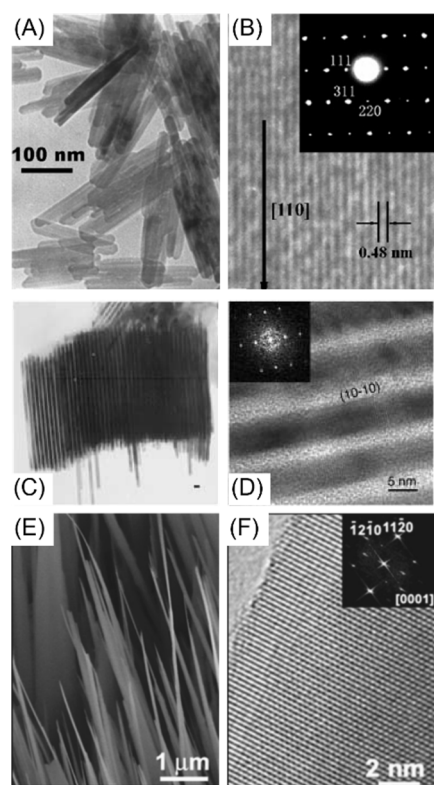
Figure 3. TEM and HRTEM images of magnetic nanorods. (A, B) Fe_3O_4 nanorods. Reproduced from ref 114. Copyright 2004 Elsevier. (C, D) Co nanorods. Scale bar in (C): 10 nm. Reproduced from ref 48. Copyright 2003 Wiley. (E, F) α-Fe_2O_3 nanowire. Reproduced from ref 115. Copyright 2006 AIP Publishing.

4.1.2. Magnetic Assembly of Nanorods.

In 2009, Ding et al. first reported the self-assembly of magnetic ellipsoids into three-dimensional (3D) superlattices through a convective method with the aid of magnetic fields.[1] The spindles of α-Fe_2O_3 (Figure 4A) with varied aspect ratios from 3 to 9 were synthesized by hydrolysis of $Fe(ClO_4)_3$. After H_2 reduction/O_2 oxidation, magnetically active γ-Fe_2O_3 spindles were obtained. However, only a nematic-like liquid-crystal phase was observed when spindles with a large aspect ratio were used for the assembly. Thus, a thick layer of SiO_2 was coated on the spindles to reduce their aspect ratio to ~1.5 (Figure 4B). The as-obtained γ-Fe_2O_3@SiO_2 ellipsoids show ferromagnetic properties with a saturated magnetization of ~7 emu/g. The shape anisotropy dominantly determines these nanorods' easy magnetization direction, largely because of the polycrystalline nature of the γ-Fe_2O_3. Under the external magnetic fields, the minimization of Zeeman energy aligns the long axis of the nanorods along the direction of the magnetic field. With the help of the magnetic field during the convective self-assembly process (Figure 4C), a 3D superlattice with both good positional (driven by the capillary force during drying) and orientational (driven by the magnetic force) orders is obtained, as shown in Figure 4D−G. Further investigation revealed that the assembled superlattice has a triclinic symmetry for the (111) plane with neighboring particles packing side-by-side (Figure 4D).

In 2015, Wang et al. reported a similar indirect method to synthesize uniform magnetic nanorods as the building blocks for self-assembly.[3] They first synthesized uniform iron oxyhydroxide (FeOOH) nanorods through a hydrothermal
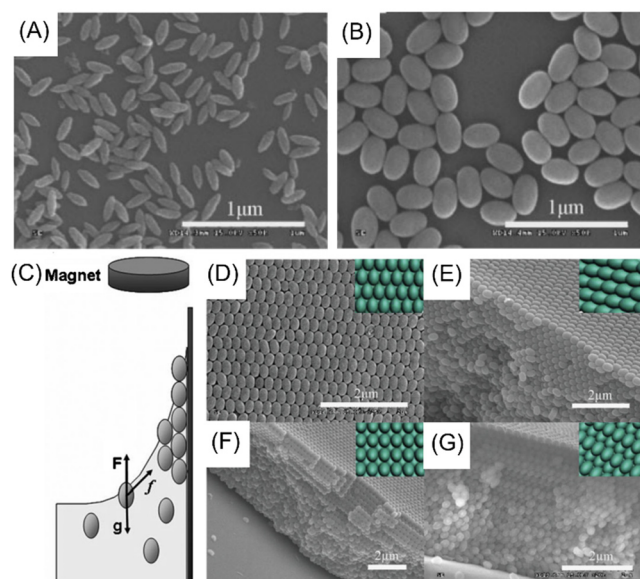
Figure 4. (A, B) SEM images of α-Fe_2O_3 (A) and α-Fe_2O_3/SiO_2 core−shell ellipsoids with an aspect ratio of 1.5 (B). (C) Schematic representation of the experimental setup for convective assembly under a magnetic field. (D-G) SEM images of different crystalline planes, with the insets showing the corresponding models. Reproduced from ref 1. Copyright 2009 Wiley.

reaction (Figure 5A). Magnetic Fe@SiO_2 ellipsoids were prepared by coating the FeOOH nanorods with a thick SiO_2
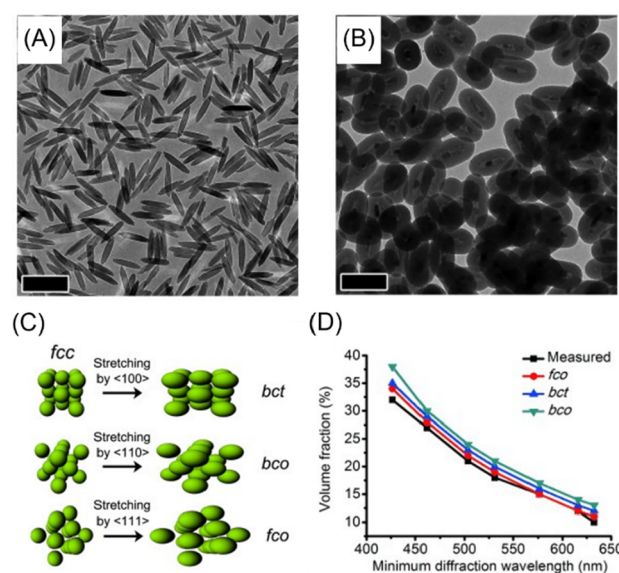
Figure 5. (A, B) TEM images of FeOOH nanorods (A) and reduced Fe@SiO_2 nanoellipsoids (B). Scale bars: 200 nm. (C) Possible structures resulting from the assembly of nanoellipsoids. (D) Measured volume fractions and the calculated values based on Bragg's law as a function of diffraction wavelength. Reproduced from ref 3. Copyright 2015 Wiley.

shell followed by H_2 reduction under 500 °C. The TEM images in Figure 5B indicate that the SiO_2 shell retains the overall ellipsoidal shape of the core after the reduction, although the Fe nanocrystals are randomly distributed in the core. The saturated magnetization of nanorods of different respect ratios is only 0.6 and 1.2 emu/g due to the thick shell
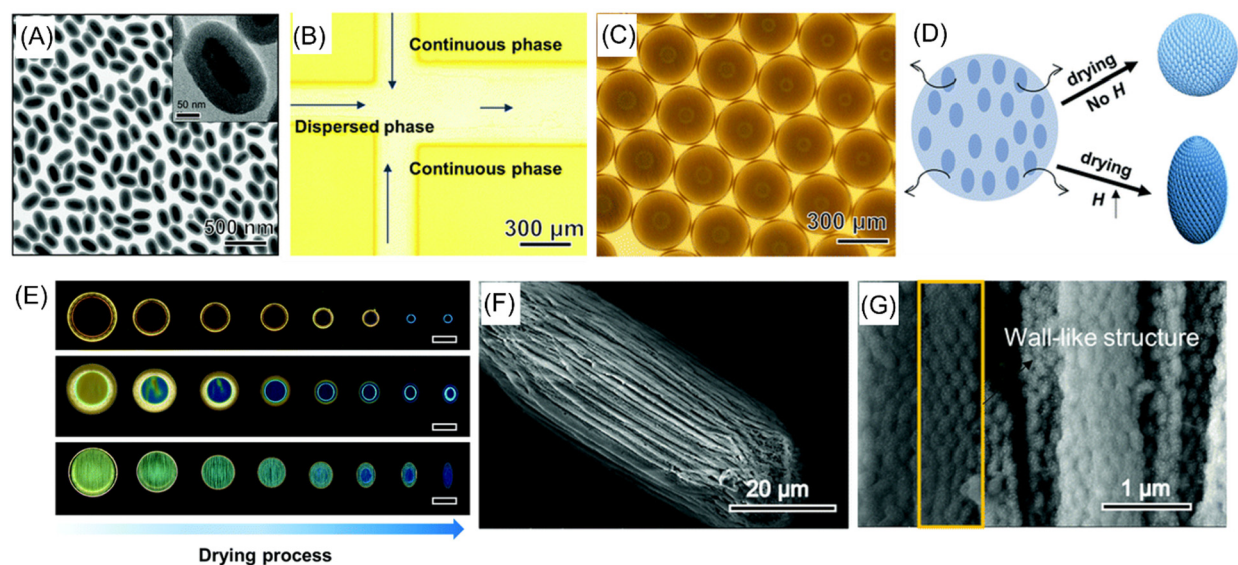
**Figure 6.** (A) TEM image of $Fe_3O_4@SiO_2$ nanoellipsoids, with the inset showing an enlarged image of one particle. (B, C) Optical microscopy images of the microfluidic device (B) and the produced aqueous droplets (C). (D) Schematic diagram of the evaporation-induced assembly processes in the absence or presence of an external magnetic field. (E) Evolution of the droplets at different drying stages (the field strength increases from top to bottom, scale bar: 100 μm). (F, G) SEM images of a broken ellipsoidal superstructure. Reproduced from ref 120. Copyright 2019 Royal Society of Chemistry.
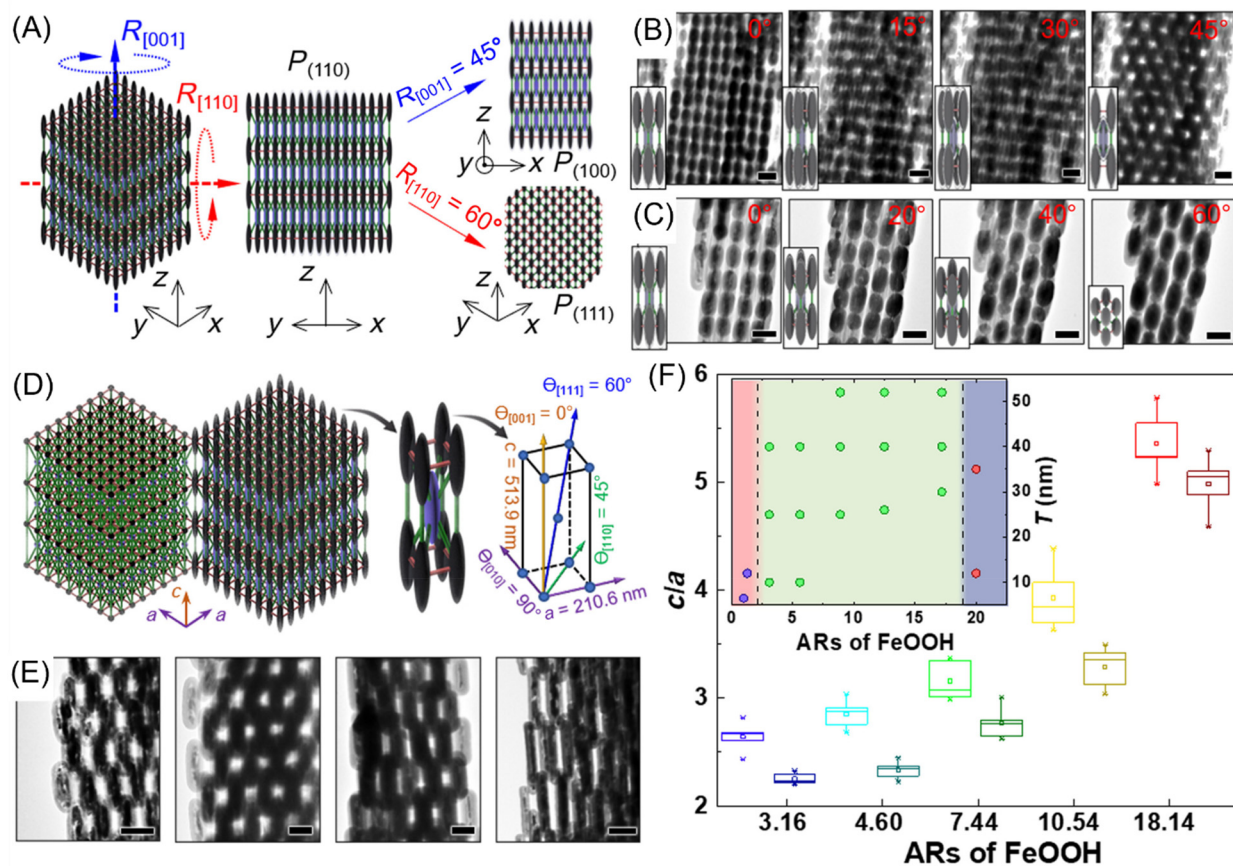
Figure 7. (A) Schematics of *bct* crystals under different orientations by rotating along given crystallographic directions. (B, C) TEM images showing *bct* crystals under various orientations by rotating along [001] (B) and [110] (C). (D) Scheme of *bct* colloidal crystals. (E) TEM images of *bct* crystals assembled from magnetic nanorods with different aspect ratios increasing from 2.25 to 18.5. (F) Dependence of the lattice constant ratio (c/a) on the aspect ratio (AR) of magnetic nanorods. Inset is the experimental phase diagram showing the magnetic assembly behaviors of rods. Blue, green, and red dots represent linear colloidal chains, *bct* crystals, and disordered fibers with only orientational orders, respectively. Reproduced from ref 2. Copyright 2021 AAAS.
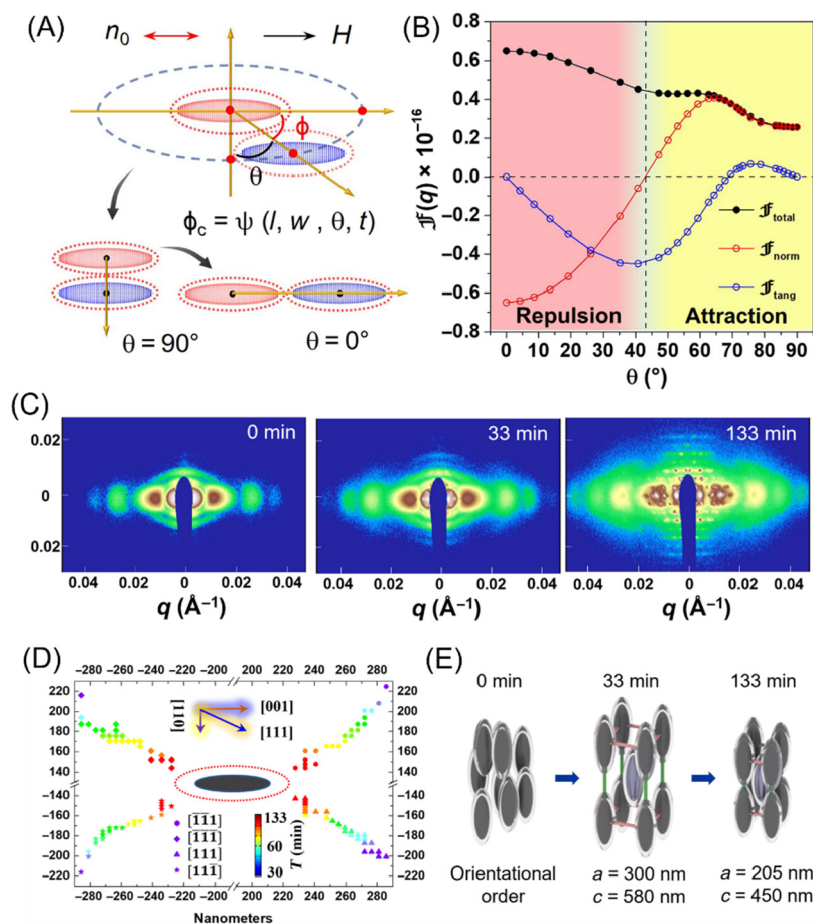
Figure 8. (A) Schematic showing the geometry for calculating the pair interaction between two nanorods under a horizontal magnetic field. (B) Plot of total force and its normal, tangent components against θ. (C) Temporal evolution of SAXS patterns measured *in situ* during the magnetic assembly of nanorods. (D) Trajectory of the magnetic nanorods during the assembly process. (E) Depiction of the magnetic assembly and formation of *bct* crystals. Reproduced from ref 2. Copyright 2021 AAAS.

of SiO_2. Considering the separation between nanorods, such a small magnetic dipole cannot induce a dipole–dipole force that is strong enough to assemble nearby particles in a dilute solution under an external magnetic field. However, as the solution becomes more concentrated (volume fraction: 10%–32%), the nanorods start packing and form an ordered structure to minimize the electrostatic repulsion caused by the significant surface charges. The as-assembled superstructure displays photonic properties, which in turn allows analyzing their order quality and crystal structure. Even though the magnetic dipole is weak, it is still sufficient to align the long axes of the nanorods along the magnetic fields. The easy magnetization direction is determined by the shape anisotropy, which is the long axis of the nanorod, most likely because of the random dispersion of Fe nanocrystal domains in the core. Such magnetic alignment not only rotates the assembled crystal structure but also reduces the defects, explaining the enhanced reflectance intensity with increasing magnetic field strength. As shown in Figure 5D, the assembled ordered structure is found to be a face-centered orthorhombic phase by calculating the diffraction wavelength using Bragg's law.

When microfluidics is combined with magnetic field-assisted assembly, uniform micron-sized superstructures can be obtained, with shapes significantly different from those obtained using regular nonmagnetic nanospheres.[116−119] Liu et al. reported that spindle-shaped microparticles could be

prepared by assembling magnetic nanoscale ellipsoids in a spatially confined oil droplet under magnetic fields.[120] The synthesis procedures of magnetic ellipsoids (Figure 6A) are similar to Ding's method.[1] Using the microfluidic-assisted evaporation-induced assembly method, the shear stress imposed by two outer oil streams (continuous phase: oil containing surfactants) on the inner thread of the dispersed phase (aqueous suspension of Fe_3O_4@SiO_2 particles) (Figure 6B) results in a periodic breakup of the aqueous stream into uniformly sized droplets (Figure 6C). Afterward, the aqueous emulsion droplets are dried under ambient conditions. The final shape of the assembled superstructures highly depends on the strength of the applied magnetic fields. In the absence of external magnetic fields, the droplet gradually shrank while keeping an overall spherical morphology during the drying. In contrast, in the presence of magnetic fields, the shrinkage along the magnetic field direction is slower than that in the perpendicular direction, eventually leading to an ellipsoidal superstructure with a higher aspect ratio under a stronger magnetic field (up to 3.2 with a field strength of 470 Oe, Figure 6E).

The formation of ellipsoidal superstructures is the result of competition between the magnetostatic energy (E_m) and the surface tension energy (E_s). During the assembly in the drying process, the magnetic fields not only align the nanoellipsoids uniformly along the magnetic field, giving rise to the good
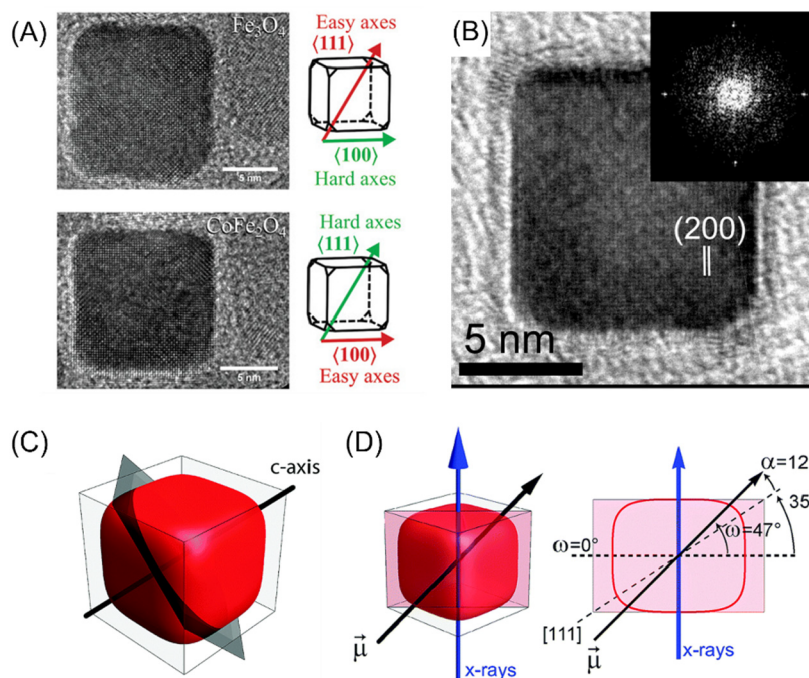
Figure 9. (A) TEM images of a Fe_3O_4 nanocube (top) and $CoFe_2O_4$ nanocube (bottom). Scale bars: 5 nm. Reproduced from ref 128. Copyright 2021 Wiley. (B) TEM image of a Ni nanocube (with an inset of FFT). Reproduced from ref 42. Copyright 2012 American Chemical Society. (C, D) Schematic illustration of the *c*-axis and c-plane (perpendicular to the *c*-axis) for a hematite microcube (C) and the spatial orientation of the magnetic dipole moment (D). Reproduced from ref 132. Copyright 2018 Royal Society of Chemistry.

orientational order, but also lead to a greater E_m due to smaller interparticle separation. In the meantime, E_s decreases because of the reduced surface area during solvent evaporation. When the droplet size decreases to a critical value, E_m dominates the total energy, leading to the deformation of the droplet. Investigating the fine structure of the assemblies revealed wall-like units with gaps in between (Figure 6F and G). Within each wall, the neighboring nanoellipsoids adopt a hexagonal packing similar to the previous findings.[1]

In the above cases, magnetic force only provides additional orientational control for the nanorods to yield a better superlattice, while other forces (i.e., capillary force and surface tension) serve as the primary driving force for assembly. Li et al. reported the self-assembly of Fe_3O_4@SiO_2 nanorods using magnetic interactions as the primary driving force.[2] The preparation of nanorods is similar to Wang's method,[3] except that the SiO_2 layer is thinner. Benefiting from that, the reduced nanorods have strong magnetic dipoles to interact with nearby nanorods, forming a highly ordered body-centered tetragonal (*bct*) superlattice (Figure 7A and B). The *c*/*a* ratio of the *bct* lattice can be easily controlled by changing the aspect ratio of the nanorods (Figure 7E and F). For example, nanorods with a length of 322 nm and width of 70 nm yield a *bct* lattice with *a* = 210.6 nm and *c* = 513.9 nm (*c*/*a* = 2.44).

The formation of the *bct* superlattice is governed by the magnetic interaction between nanorods, which is analyzed using the finite element method. As shown in Figure 8A and B, the magnetic force between two contacting nanorods can be divided into one along the normal direction and the other along the tangent direction with respect to the contact point. The normal force describes whether the force is repulsive or attractive, while the tangent force describes if the nanorods tend to assemble along the tangent direction. The energetically most stable configuration is achieved when the normal force is

attractive and the tangent force is 0. Interestingly, instead of a head-to-end configuration (metastable state), the energy minimum is found when there is a critical angle between the short axis of the nanorods and the line connecting the centers of two nanorods. Depending on the SiO_2 shell thickness and the aspect ratio of the nanorods, this critical angle originates from the magnetic interaction among nanorods and forms the *bct* superlattice.

The formation kinetics of the superlattice is investigated by *in situ* synchrotron-based small-angle X-ray scattering (SAXS) (Figure 8C). At 0 min, the anisotropic scattering pattern implies the liquid crystal phase of nanorods with only orientational orders and parallel alignment to a vertical magnetic field. At 133 min, a well-defined rectangular diffraction pattern formed, confirming the perfect structure of the *bct* lattice. Figure 8D shows the evolution of local rod position along [111] crystallographic directions, indicating nearly linear spatial lattice contraction.

4.2. Nanocubes

4.2.1. Easy Magnetization Direction of Nanocubes.
There are many reported methods for the direct synthesis of magnetic nanocubes with sizes ranging from nanometer to submicron, with compositions including Fe,[37−40,121] α-Fe_2O_3,[122,123] Fe_3O_4,[59−61,93] FePt,[51,52] Ni,[42] $MnFe_2O_4$,[124−126] and $CoFe_2O_4$.[127,128] The most employed direct synthesis method is based on the thermal decomposition of organometallic compounds at high temperatures in organic solvents, using ligands to bind stronger on (100) than on (111) or (110) facets of the crystal with cubic symmetry and promote the growth along [111] or [110] rather than [100] direction.[59,129] Nanocubes synthesized using this method are usually single-crystalline or quasi-single-crystalline. In contrast, indirect synthesis methods often yield nanocubes with polycrystalline structures.[93,130,131]
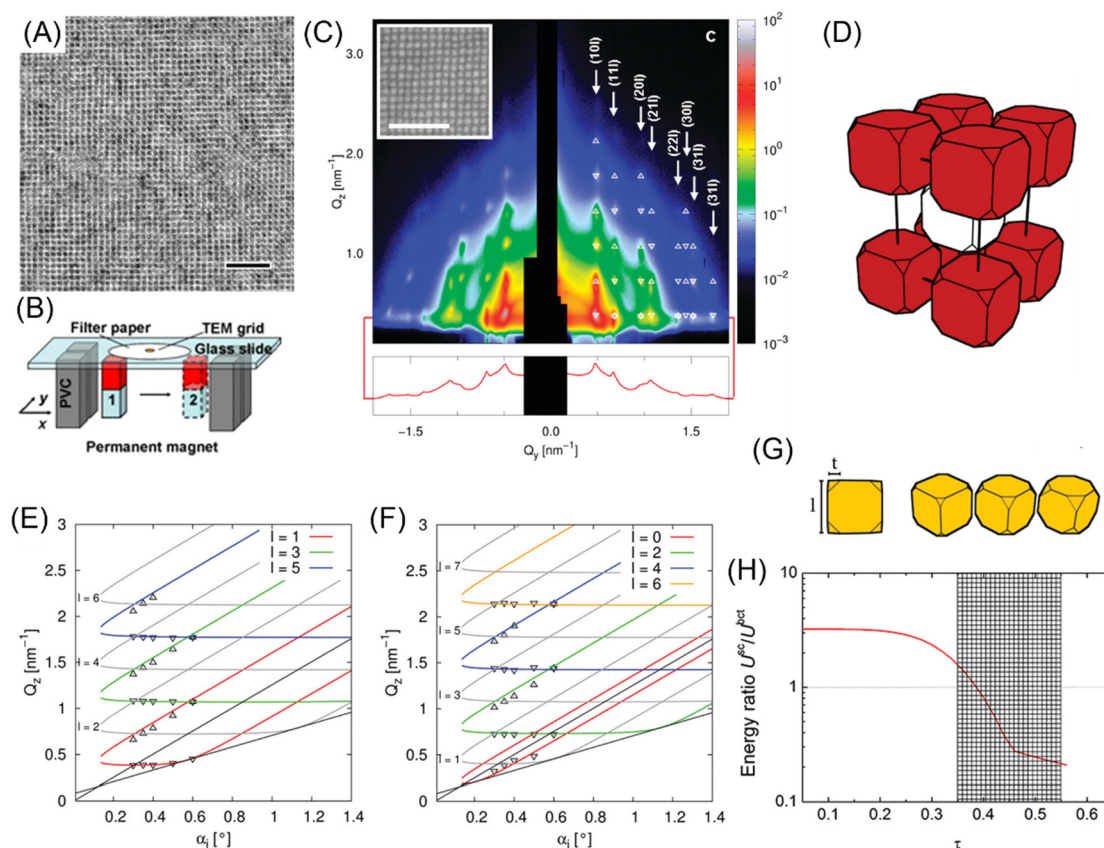
Figure 10. (A) TEM image of magnetic-field-induced self-assembly of maghemite nanocubes into an oriented superlattice (scale bar: 100 nm). (B) Schematic illustration of the experimental setup for magnetic assembly. Reproduced from ref 134. Copyright 2007 The National Academy of Sciences of the USA. (C) GISAXS patterns of assemblies of iron oxide nanocubes (inset: the corresponding SEM images, scale bar: 100 nm). (D) Schematic illustration of the assembled *bct* superlattice. (E, F) The (10l) (E) and (11l) (F) reflection series as observed by GISAXS. (G) Schematic illustration of the dimensionless degree of truncation τ and representation of nanocubes with varying τ. (H) Ratio between the interaction energies of a truncated cube in a *sc* and *bct* lattice. Reproduced from ref 135. Copyright 2011 American Chemical Society.

The magneto-crystalline easy axis of most magnetic nanocubes is along their [111] crystallography direction owing to their negative K_{c1}, including Fe_3O_4 (Figure 9A, top), $\gamma\text{-}Fe_2O_3$, and most ferrites ($MnFe_2O_4$, $NiFe_2O_4$, etc.). These directions coincide with the body diagonals of the single-crystalline nanocubes. However, $CoFe_2O_4$, with a positive K_{c1}, is an exception in ferrites with its magneto-crystalline easy axis along the [100] crystallography direction (Figure 9A, bottom). Magneto-crystalline anisotropy of ferrites originates from the spin−orbit interaction of the bivalent cations. For most bivalent cations (Mn^{2+}, Ni^{2+}, Cu^{2+}, Zn^{2+}, Mg^{2+}, and Cd^{2+}), the orbital moment is quenched, resulting in a relatively small magneto-crystalline anisotropy. The Co^{2+} case is different because it has an orbital moment of the same magnitude as the spin moment, which induces a large magneto-crystalline anisotropy constant.[70]

Hematite ($\alpha\text{-}Fe_2O_3$) is another special magnetic material despite its weak magnetic property, with the spontaneous magnetization of 2.2×10^3 A m^{-1} (vs 4.8×10^5 A m^{-1} for Fe_3O_4).[132] Different from Fe_3O_4 with the spinel crystal structure, $\alpha\text{-}Fe_2O_3$ has a rhombohedral lattice that belongs to the trigonal crystal system. When $T_M < T < T_N$ (T_M: Morin temperature, ~263 K; T_N: Neel temperature, ~953 K), $\alpha\text{-}Fe_2O_3$ exhibits a nonzero spontaneous magnetization perpendicular to its *c*-axis due to canting of the magnetic spins away from the [0001] direction toward the basal plane.[133] Because of its low saturated magnetization, only $\alpha\text{-}Fe_2O_3$ particles with

sizes of submicron/micrometers exhibit decent magnetic interaction. Hematite cubes with sizes ranging from hundreds of nanometers to several micrometers can be synthesized by a simple hydrothermal reaction.[56] These single crystalline microcubes have their *c*-axis along one of their body diagonals (Figure 9D), resulting in an easy axis in the plane perpendicular to this body diagonal in terms of magneto-crystalline anisotropy.[132]

4.2.2. Magnetic Assembly of Nanocubes. The superstructures obtained from the assembly of magnetic nanocubes are of particular interest due to their packing factor reaching up to 1 (as opposed to spheres, which can be packed to a maximum factor of 0.74), which allows for coupling as strong as possible between the nanoscale building blocks.

Ahniyaz et al. assembled the single-crystalline truncated Fe_3O_4 nanocubes with an edge length of 9 nm in the liquid−air interface using a drying-mediated method in the presence of magnetic fields.[134] The magnetic fields play an important role in controlling the orientation of nanocubes during the assembly process and significantly affect the assembled structures. When nanocubes are allowed to assemble without magnetic fields, mosaic-like particle arrays are obtained after drying, while highly ordered, virtually defect-free superlattices are created by subjecting the drying dispersion to a vertical magnetic field. The nanocubes in the superlattice adopt a face-to-face arrangement with a separation distance of 3.7 nm to accommodate the oleate ligands (Figure 10A). The duration of
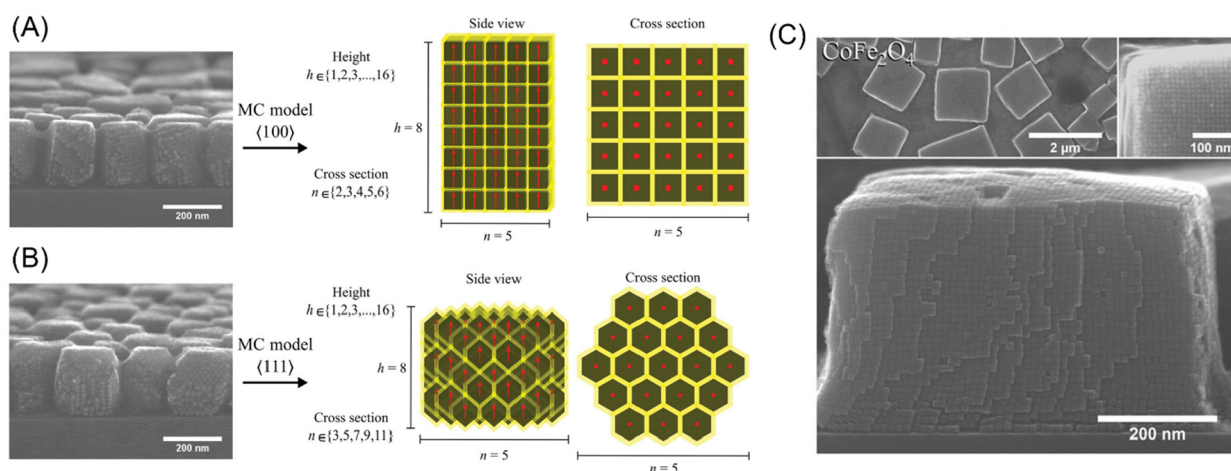
Figure 11. (A, B) SEM images and the corresponding simulation models of assembled superlattices of Fe_3O_4 nanocubes with face-to-face packing (A) and corner-to-corner packing (B). Reproduced from ref 89. Copyright 2019 Wiley. (C) SEM images of $CoFe_2O_4$ superlattices. Reproduced from ref 128. Copyright 2021 Wiley.
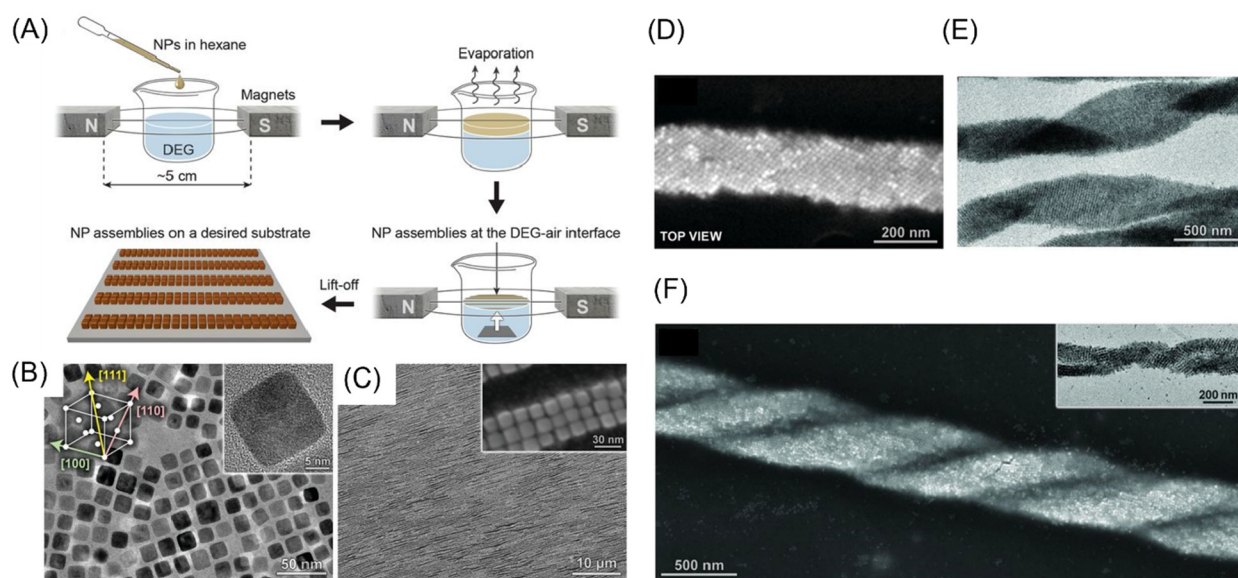
**Figure 12.** (A) Schematic representation of the experimental setup for magnetic assembly. (B) TEM images of Fe_3O_4 nanocubes. (C−E) SEM images of assembled 1D belts with [100] packing (C), [110] packing (D), and single-stranded helices with [111] packing (E). (F) SEM image of a well-defined double helix, with the inset showing a TEM image of two belts wrapping around each another. Reproduced from ref 136. Copyright 2014 AAAS.

the applied magnetic field also affects the structure of the superlattice. Nanocubes tend to form large and ordered thin arrays by applying a vertical magnetic field during the initial phase of the assembly process; however, if the magnetic field is applied for the entire assembly process, micrometer-sized and thick three-dimensional superlattices are obtained.

The mechanism for assembling magnetic nanocubes was conjectured based on the experimental observations. The mosaic-like array formed without a magnetic field suggests the first formation of small, ordered clusters and then the fusion of each domain into large, disordered arrays. When the magnetic field is only applied during the initial phase of the assembly process, the additional dipole−dipole interaction promotes the formation of a cluster beyond a critical size. Such a cluster serves as a nucleus for the subsequent growth of highly ordered superlattice when the magnetic field is removed, leading to the formation of thin arrays. If the magnetic field is applied

throughout the drying process, the dipole−dipole interaction stacks the nanocubes on top of the cluster due to the vertical magnetic field, resulting in thick three-dimensional superlattices.

Although the nanocubes are packed face-to-face in the superlattice, the exact crystal phase of the obtained superlattice was not revealed in Ahniyaz's work.[134] In 2011, Disch et al. investigated the three-dimensional structure of the superlattice by combining grazing incidence small-angle scattering (GISAXS) and electron microscopy.[135] The in-plane square lattice has a lattice constant of $a = 13.10$ nm, confirmed in the SEM image and by the GISAXS measurement (Figure 10C). Based on the (10l) and (11l) reflection series as observed by GISAXS, the full 3D superlattice structure is determined to be body-centered tetragonal (bct) with a lattice constant $c = 17.80$ nm (Figure 10E and F). Other than the experimental determination of the superlattice structure, the author also
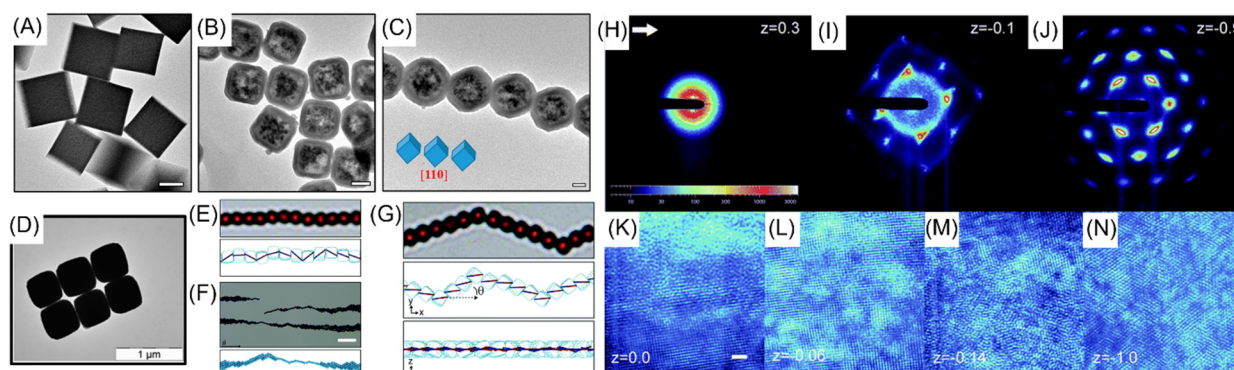
Figure 13. (A, B) TEM images of nanocubes of PB (A) and $Fe_3O_4@SiO_2$ (B). Scale bars: 100 nm. (C) TEM image of a 1D chain assembled with [110] packing. Scale bars: 100 nm. Reproduced from ref 93. Copyright 2019 American Chemical Society. (D) TEM image of hematite microcubes. Reproduced from ref 56. Copyright 2013 Royal Society of Chemistry. (E−G) Experimental observations and computer simulations of hematite microcube assemblies under magnetic fields, with the field strength increasing from (E) to (G). Scale bar in (F): 20 μm. Reproduced from ref 132. Copyright 2018 Royal Society of Chemistry. (H−N) μrad-XRD patterns (H−J) and HXRM images (K−N) of the hematite sediment assembled in the presence of a magnetic field. Scale bar in (K): 3 μm. Reproduced from ref 56. Copyright 2013 Royal Society of Chemistry.

built a model based on the energies of superstructures (the energy it requires to remove a nanocube) to investigate the influence of truncation degree on the superlattice structure. The model indicates that at low truncations ($\tau < 0.4$), the simple cubic (sc) lattice is more stable than the body-centered tetragonal (bct) lattice, and there is a sc to bct transition as the degree of truncation increases (Figure 10H). This structural transformation is driven by the rapidly growing van der Waals (vdW) attraction along the bct diagonal as the degree of truncation increases. Since the nanocubes used in the experiment have a truncation of 0.45, the bct lattice is more energetically favored, which is consistent with the theoretical studies.

Superlattice with a packing manner other than face-to-face was reported by Håkonsen et al. using a similar experimental setup.[89] Two different packing arrangements of nanocubes within the superstructures were found, with face-to-face or corner-to-corner packing along the vertical direction (magnetic field line) (Figure 11A and B). Compared with the bct lattice with face-to-face packing, the appearance of corner-to-corner arrangements is presumably due to the stronger magnetic field applied (120 mT vs 30 mT), making dipole−dipole interaction (which favors corner-to-corner packing) comparable or even stronger than the vdW interaction (which favors face-to-face packing). Although face-to-face packing arrangement was also observed, its origin was ascribed to the local nanocube concentration and magnetic field gradient. When $CoFe_2O_4$ nanocubes of the same sizes were employed as building blocks for the assembly using the same method, superlattices with only face-to-face packing (Figure 11C) were obtained because of the cooperation of dipole−dipole interaction ([100], the easy magnetization direction) and vdW interaction.[128]

More interesting and complex superstructures, including one-dimensional belts and single, double, and triple helices, could be obtained when the magnetic field is parallel to the liquid−air interface during the evaporation-induced self-assembly using monodisperse magnetite nanocubes with an average edge length of 13.4 nm and corner bluntness of 23% as building blocks (Figure 12B).[136] The assembled super-structures were highly dependent on the surface concentration (χ) of the particles. When $\chi < 0.2$, no long-range or well-defined structures were found. When $\chi = \sim0.2$, NCs assembled into parallel arrays of one-dimensional (1D) belts with a width

of two to three NCs across and length up to 100 um (Figure 12C) oriented parallel to the applied field. Within these belts, individual cubes had their [100] crystallographic axes oriented parallel to the long axes of the belts. When $1 < \chi < 1.5$, 1D belts were still observed. However, the cubes in the belts had their [110] axes oriented parallel to the long axes of the belts (Figure 12D). When $\chi = \sim1.5$, as shown in Figure 12E, the cubes oriented their [111] along the magnetic field lines, and the belts spontaneously folded, giving rise to single-stranded helices. The relatively thin helices prepared at $1.5 < \chi < 2.0$ comprised equal populations of intermixed left- and right-handed structures, all oriented parallel to the applied field. However, at higher ($\chi > 2.0$) coverages, long axes of the helices were tilted with respect to the external field, with the tilt angles increasing with increasing χ values.

The formation of various superstructures at different surface concentrations is explained by the interplay of vdW interaction and dipole−dipole interaction. When χ is low (0.2−1), vdW interaction dominates, and nanocubes are presumably magnetized along their hard axes ([100]) to minimize the total energy. As χ increases to 1−1.5, the belts become wider, and the parallel arrangement of magnetic dipoles increases the energy of the belts, which decreases the stability of the superstructures. The nanocubes are then magnetized along the intermediate axes ([110]) to decrease the magnetic energy in the compensation of compromised vdW interaction. When χ is even higher (>1.5), the nanocubes are magnetized along their easy axes ([111]) because of the large effective magnetic field generated by a large number of nanocubes, forming helical belts. Monte Carlo simulations confirm that the formation of helices is accompanied by free energy minimization. Further analysis reveals that the helices originate from the packing of chiral nanocube nuclei, resulting from the competition of magnetic and spatial symmetries. The helical belts also exhibit other interesting features, such as helices with the same handedness on a large scale and domains with inverted helices (collective switching of chirality).

Different from the assembly during the drying process, the assembly of magnetic nanocubes in solutions results in different superstructures. Li et al. reported the synthesis of $Fe_3O_4@SiO_2$ nanocubes with an overall length of ~250 nm through an indirect method: a layer of SiO_2 was first coated on the presynthesized Prussian blue nanocubes (Figure 13A), and

the resulting core−shell nanoparticles were then reduced into magnetic $Fe_3O_4@SiO_2$ in polyol at high temperature.[93] Due to the shrinkage of Prussian blue by reduction, the nanocube core consists of randomly distributed nanocrystals with a size of ∼10 nm (Figure 13B), making these nanocubes superparamagnetic despite their large dimension. Under the magnetic field, the dipole−dipole interaction drives the nanocubes into forming 1D single chains within which most of the nanocubes tend to align edge-to-edge (Figure 13C), with a few face-to-face and corner-to-corner defects. Since the crystal domains are randomly distributed and orientated in the core, the magneto-crystalline anisotropy can be negligible in determining the easy magnetization direction. Considering shape anisotropy, the longest axis is easier to be magnetized due to the lower demagnetization factor, which occurs to be the body diagonals of the nanocubes. However, the corner-to-corner arrangement is not favored in terms of the vdW interaction due to the small contact area. The competition between these two interactions eventually results in a compromised edge-to-edge arrangement in the chains.

Aside from the most investigated Fe_3O_4 nanocubes, the assembly of α-Fe_2O_3 microcubes has also been studied, for example, using those with round corners and average edge lengths varying between 500 and 1500 nm.[56] By investigating the superstructure formed by gravity-facilitated sedimentation in the presence of a magnetic field using SAXS, the dipole moment in the hematite cubes is determined to be situated at an angle $a = 12°$ into the cube's face with respect to its body diagonal (Figure 9E).[132] When the cubes are confined inside flat glass capillaries, they simultaneously assemble into 1D or quasi-2D structures with an applied magnetic field, and the structures depend on the magnetic field strength and concentration of particles. In a weak magnetic field, the cubes attached face-to-face to form straight 1D long chains (Figure 13E). As the field strength became stronger, the increased Zeeman interaction was strong enough to align all the dipoles along the magnetic field. At the same time, the chains buckled and evolved into kinked structures with a well-defined angle (Figure 13F). If the particle concentration increased, the chains started to interact with each other and assembled into bundles (Figure 13G). Theoretical investigation reveals that the kinks are energetically unfavored since they destabilize the chains by the unfavorable orientation of the cube that connects the two sides of the chain. However, the formation of kinks causes an entropy gain of the cluster, which is an entropically driven process. Similar kinked chains have also been observed by Aoshima et al.[137]

The superlattice of hematite cubes resulting from the sedimentation in the presence of a magnetic field has been previously determined by Meijer et al. in 2013.[56] The magnetic field is employed to provide an orientational control during the sedimentation, facilitating the formation of highly ordered superlattice over a long-range (Figures 13H−N). The cubes at the tope region of the sediment are found to assemble into base-centered monoclinic lattice, with lattice parameters of a = 846 nm, b = 852 nm, and c = 972 nm with $\alpha = \beta = 90°$ and $\gamma = 85°$.

4.3. Nanoplates

4.3.1. Easy Magnetization Direction of Nanoplates.
Considering shape anisotropy, the easy magnetization direction of plate-shaped particles lies in the basal plane due to their larger diameter compared with their thickness.[5]

However, the overall easy magnetization direction is highly dependent on the crystal domain size and crystal phase of the particles. Yang et al. synthesized hexagonal Fe_3O_4 nanoplates through a two-step method (Figure 14A).[138] The α-Fe_2O_3
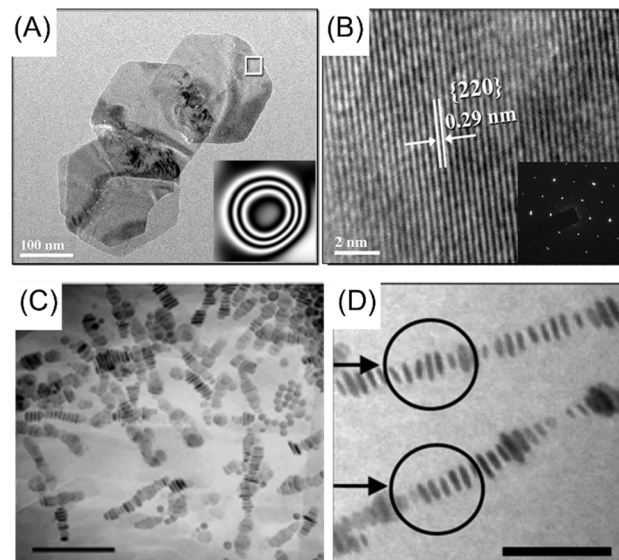


Figure 14. (A) TEM image (inset: electron holography of a single nanoplate). (B) HRTEM of a reduced hexagonal Fe_3O_4 nanoplate (inset: SAED image). Reproduced from ref 138. Copyright 2015 Wiley. (C, D) TEM of Co nanoplates (C, scale bar: 100 nm) and their face-to-face assembly under a magnetic field (D, scale bar: 200 nm). Reproduced from ref 46. Copyright 2002 American Chemical Society.

nanoplates were synthesized and then reduced into Fe_3O_4 in a trioctylamine and oleic acid mixture. Such a hydrogen-wet reduction method avoided the shape damage and coalescence usually occurring in the gas phase reduction. Although there was no sufficient evidence showing the reduced nanoplates were single crystalline, the crystal domains with a lattice spacing of the (220) plane of inverse spinel Fe_3O_4 could be identified within the basal plane (Figure 14B). In this case, both magneto-crystalline and shape anisotropy support an easy magnetization direction in the basal plane, resulting in the parallel alignment of nanoplates along the magnetic fields.

For magnetic materials of the hexagonal crystal system, single crystal nanoplates are usually obtained by the limited growth along their c-axis. The easy magnetization direction in terms of magneto-crystalline anisotropy is perpendicular to that of shape anisotropy. Many materials possess a large uniaxial magneto-crystalline constant that dominates over the shape anisotropy effect, making their easy magnetization direction perpendicular to the basal plane (i.e., Co[46,139] in Figure 14C and D and Hexaferrites[140−143]).

4.3.2. Magnetic Assembly of Nanoplates.
The self-assembly of nanoplates under magnetic fields has been less studied compared with that of nanorods and nanocubes. The possible reason could be the need for controlling two degrees of freedom simultaneously to fully control the orientation of the nanoplates.

Recently, Zhang et al. synthesized uniform core−shell Ni@SiO₂ nanoplates by reducing the $Ni(OH)_2@SiO_2$ in H_2 gas.[144] The core of nanoplates has a dimeter of 126 nm and a thickness of ∼20 nm with a 50 nm SiO_2 shell (Figure 15A and
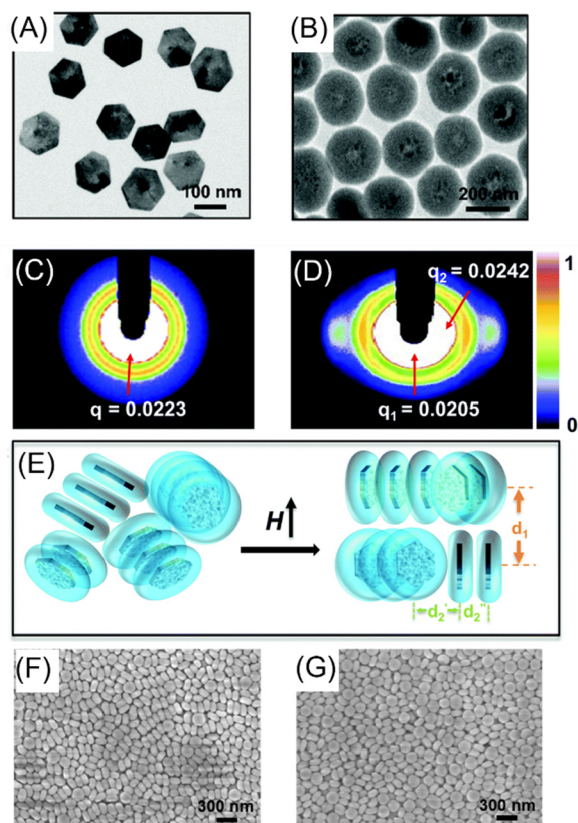
Figure 15. (A, B) TEM images of Ni(OH)$_2$ (A) and Ni@SiO$_2$ (B) nanoplates. (C, D) SAXS pattern of the nanoplate dispersion in the absence of magnetic field (C) and under a vertical magnetic field (D). (E) Schematic illustration of the possible structural change after applying a vertical magnetic field. (F, G) SEM images of assembled superstructures drying on the substrate with a vertical (F) and parallel (G) magnetic field. Reproduced from ref 144. Copyright 2020 Royal Society of Chemistry.

B). Their method for assembling nanoplates under magnetic fields was similar to that of Wang et al.[3] Upon increasing the particle concentration to above a critical value, only local crystalline structures were formed due to the lack of long-range orientational control of the nanoplates, which can be seen from the ring pattern in the SAXS measurement (Figure 15C). When a magnetic field was applied vertically, the SAXS pattern showed 2 peaks (Figure 15D), corresponding to a lattice spacing of 305 nm in the vertical and 260 nm in the horizontal direction. Compared with the previous pattern (with a spacing of 282 nm in both directions), the stretching of the spacing in the vertical direction implies that the magnetic field could help nanoplates form a long-range ordered structure along the direction of the magnetic field. The SEM images in Figure 15F and G show that the superstructure has many defects likely caused by the insufficient magnetic response of the nanoplates (saturation magnetization: 0.63 emu/g) and the additional degree of freedom allowing the nanoplates to rotate around their magnetization axis.

4.4. Peanut-Shaped Particles

The synthesis of peanut-shaped α-Fe$_2$O$_3$ microparticles was first reported by Sugimoto et al. in 1993.[145] Their magnetic field-induced assembly behavior was studied by Lee and Liddell in 2009.[133] The peanut-shaped particles with a length of 2.6 μm and lobe diameter of 1.18 μm are composed of many

acicular crystallites, all roughly oriented along the particle's major axis but with some radial splay, particularly in the two constituent lobes, as shown in Figure 16C. The HRTEM image shows that the major axes of the crystallites coincide with the hematite c-axis. Even though the peanut-shaped particles are not single crystalline, the identical orientation of the crystallites makes the whole particle possesses an "overall" crystalline anisotropy and creates a magnetic dipole oriented in a transverse direction to the particle's major axis (in the plane perpendicular to the c-axis) (Figure 16A). Under the magnetic field, the peanut-shaped particles assemble into kinked chains along the magnetic field in a confined 2D cell (Figure 16E). Within the chains, the major axes of the particles are perpendicular to the field lines due to the Zeeman interaction. The assembly of peanut-shaped particles without confinement forms chains with random crisscrosses linked to adjacent particles primarily at the waist (side-by-side, Figure 16D). When the concentration of particles is increased, a nearly dense monolayer of oriented particles with some vacancy defects (Figure 16F) is formed by the coalescence of individual zigzag aggregates under 2D confinement conditions. The ordered monolayer has an oblique lattice with a = 1.33 μm and b = 2.82 μm, and an interaxial angle γ of 122° (Figure 16G).

The same group then studied the assembly behavior of these peanut-shaped particles after they reduced the α-Fe$_2$O$_3$ into Fe$_3$O$_4$.[146] While the overall particle shape was preserved after reduction, the acicular crystallite microstructure was lost due to the crystal lattice change from rhombohedral to cubic (Figure 16H and I). As a result, the magneto-crystalline anisotropy is diminished, and the easy magnetization direction is predominantly determined by the shape anisotropy. When a magnetic field is applied, the peanut-shaped particles align their major axis along the magnetic field, forming chains with end-to-end attachment (Figure 16J and K).

4.5. Hybrid Particles

In the above examples, the outer layers (mainly SiO$_2$) are relatively uniformly coated on the nanoparticles, so the core particles' original shapes remain unchanged. However, the symmetries of the cores can be broken when the shells are anisotropically coated. Although the nonmagnetic layers do not contribute to the magnetic anisotropy, the assembly behaviors of these hybrid particles can still significantly deviate from the bare core particles due to the additional anisotropic steric hindrance originating from the outer layers.

Ge et al. reported the synthesis of Fe$_3$O$_4$@SiO$_2$@ Polystyrene (PS) composite colloids with anisotropic structures.[147] The particles are produced by one-step emulsion polymerization of styrene using Fe$_3$O$_4$@SiO$_2$ as seeds. The interfacial tension between the hydrophilic seed particle and the hydrophobic monomer is the key to the formation of eccentric core−shell particles (Figure 17A). By increasing the concentration of the monomer or performing a two-step coating strategy, ellipsoidal particles with the magnetic core eccentrically located at one end (Figure 17B) or doublets containing two spheres (Figure 17C) can be obtained, respectively. Unlike magnetic particles with concentric core− shell structures forming straight chains under magnetic fields (Figure 17D), the assembly of eccentric particles produces zigzag chains (Figure 17E), within which the magnetic cores are brought to the nearest locations relative to each other. This configuration is the competing result of steric hindrance and magnetic dipole−dipole attractions. Similar zigzag chains were
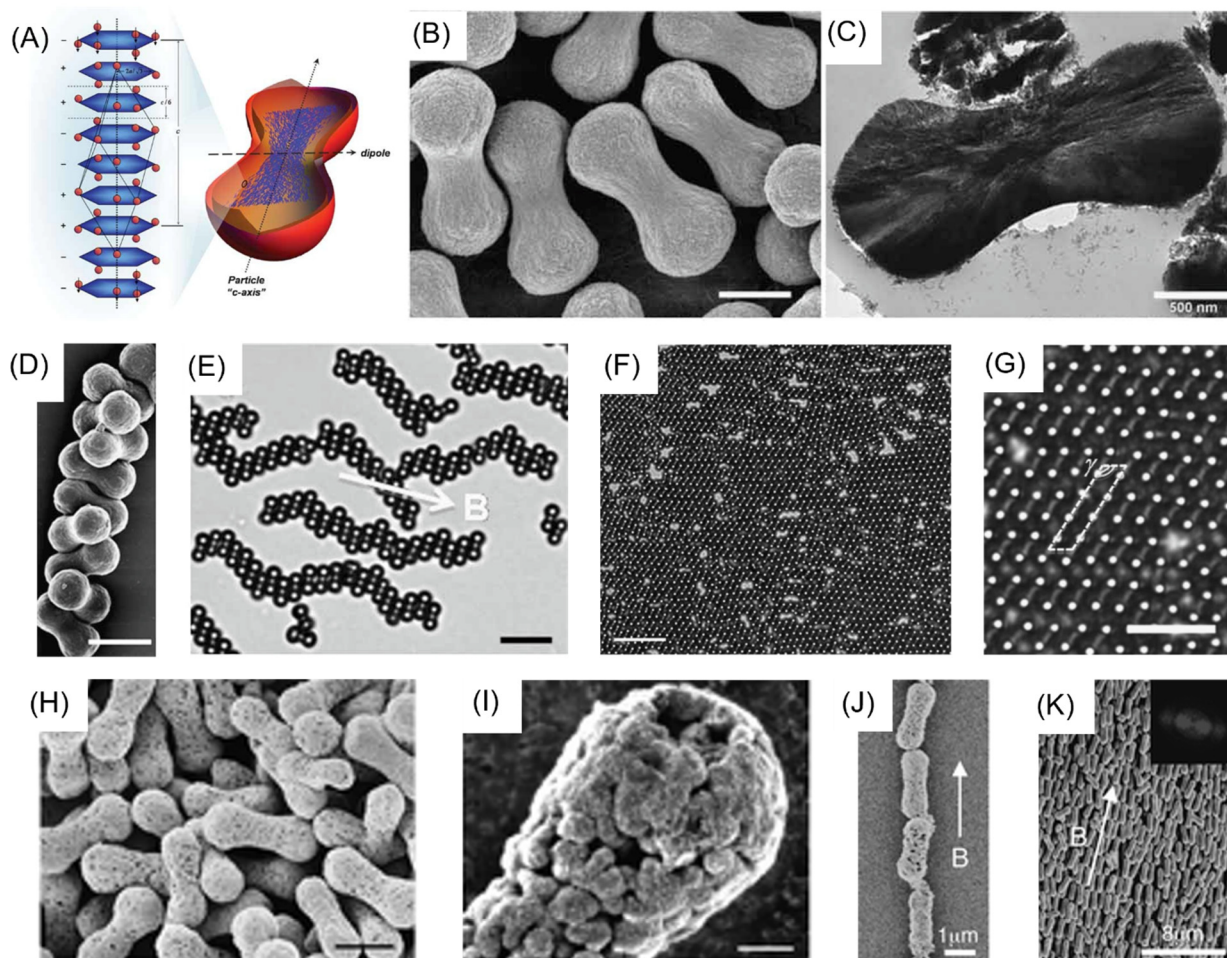
Figure 16. (A) Scheme showing the crystal structure of a hematite crystallite and the peanut-shaped colloids. (B, C) SEM and TEM images of hematite peanut-shaped colloids. Scale bar in (B): 1 μm. (D) SEM image of particle chains formed upon drying. Scale bar: 2 μm. (E) Optical image of planar, kinked zigzag chains under 2D confinement. Scale bar: 5 μm. (F, G) Optical images of the monolayer oblique superlattices. Scale bar in (F): 10 μm and (G): 5 μm). Reproduced from ref 133. Copyright 2009 Wiley. (H, I) SEM images of the particles after reduction into magnetite. Scale bar in (H): 1 μm and (I): 200 nm. (J, K) SEM images showing the orientation of the reduced particles after drying under a magnetic field. Reproduced from ref 146. Copyright 2009 Royal Society of Chemistry.

also reported by Smoukov et al. using magnetic Janus particles prepared by partially coating one hemisphere of PS microspheres with a thin layer of Fe.[94]

In 2016, Zhao et al. reported the synthesis of Janus rods through the unidirectional growth of SiO_2 on one side of Fe_3O_4 spherical seeds (Figure 17F).[148] Such an unusual growth of SiO_2 is believed to result from the uneven deposition of H_2O droplets on the seed surface. The morphology of the Janus rods, such as length and diameter, is affected by multiple parameters, including seed size, reaction time, temperature, and reagent concentrations. For example, when the temperature gradually decreases during the synthesis, particles with the chess-piece shape shown in Figure 17G are obtained due to the changing reaction rate during the growth. When the magnetic field is applied, the magnetic tips form 1D chains with silica rods swaying randomly aside the main chain (Figure 17H). However, when the Janus rods are modified with a thin hydrophobic shell, due to the hydrophobic–hydrophobic attraction between neighboring rods, the rods tend to stay on the same side of the main chain under the same magnetic field (Figure 17I).

Particles with a bicone shape can be prepared by stretching the spherical $Fe_3O_4@SiO_2@PS$ core–shell particles at a high temperature.[149] The aspect ratio of the bicone-shaped particles can be easily tuned by the draw ratio during the thermal stretching, as shown in Figure 17J. In order to better image the particles under an optical microscope, the cores and the shell were labeled with rhodamine isothiocyanate and fluorescein isothiocyanate dyes, respectively. The particles can be assembled into ordered superlattices by the depletion force induced by a depletant (Sodium polystyrenesulfonate) (Figure 17K). These superlattices begin to melt upon applying a magnetic field, eventually forming string structures along the magnetic field direction (Figure 17M), driven by the magnetic dipole–dipole interaction discussed in Section 3.

The anisotropic coating can be formed on not only spherical cores but also magnetic microcubes. Sacanna et al. reported the eccentric coating of hematite microcubes by an organo-silica polymer shell (Figure 18A).[150] The key to obtaining particles with such a morphology is that the microcubes serve as nucleation sites, inducing the formation of oil droplets resulting from the polycondensation reaction between metastable water-soluble silanols. Due to the permanent
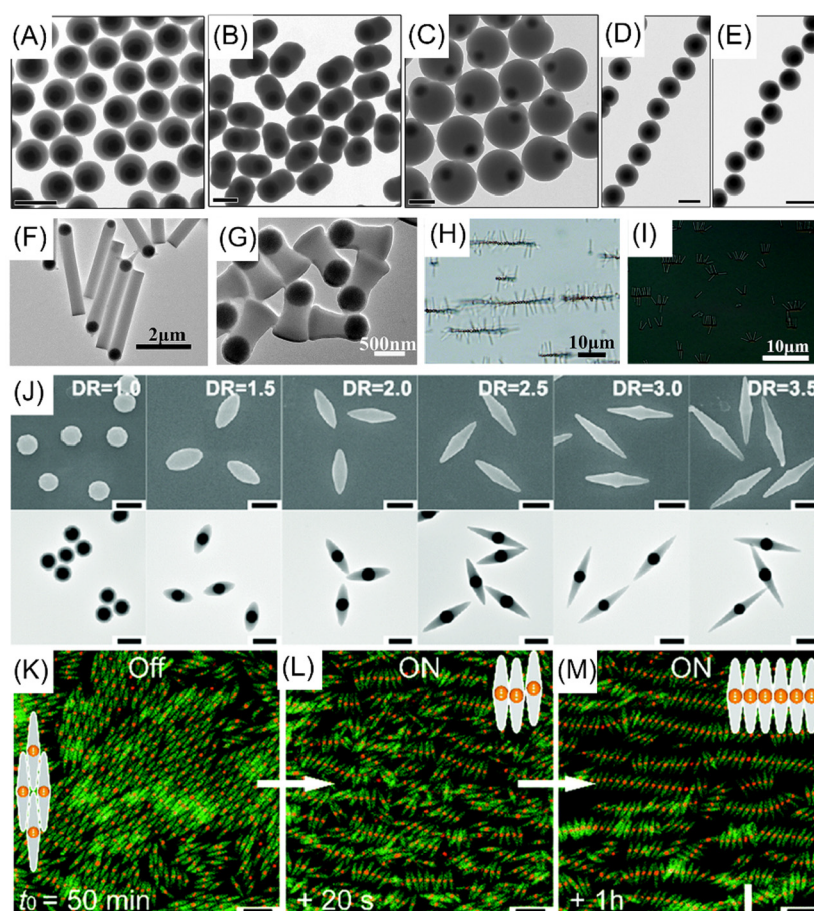
Figure 17. (A−C) TEM images of Fe$_3$O$_4$@SiO$_2$@PS composite particles with eccentric (A), ellipsoidal (B), and doublet (C) shapes. Scale bars: 400 nm. (D, E) TEM images of assembled chains of concentric (D) and eccentric particles (E) under magnetic fields. Scale bars: 400 nm. Reproduced from ref 147. Copyright 2007 American Chemical Society. (F) TEM image of matchstick-shaped (F) and chess piece-shaped (G) Janus rods. (H, I) Optical microscopic images showing the directed assembly of the Janus rods into chains under an external magnetic field before (H) and after (I) hydrophobization. Reproduced from ref 148. Copyright 2016 Royal Society of Chemistry. (J) SEM and TEM images of bicone-shaped Fe$_3$O$_4$@SiO$_2$@PS colloidal particles with increasing draw ratios from 1.0 to 3.5. Scale bars: 1 μm. (K−M) Optical microscopic images of the assembled superlattices from bicone-shaped particles with (K) and without (M) the magnetic field. Scale bars: 5 μm. Reproduced from ref 149. Copyright 2020 Royal Society of Chemistry.
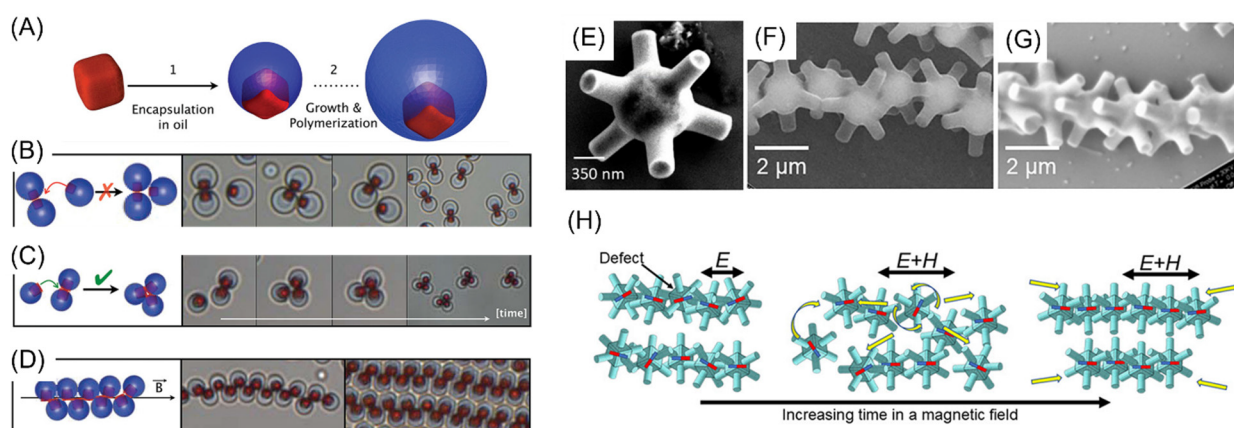
Figure 18. (A) Schematic diagram showing the synthetic steps of hematite microcube encapsulated organo-silica polymer sphere. (B, C) Magnetic-click colloidal assembly of dimers (B) and trimers (C) without magnetic fields. (D) Zigzag chains formed upon the application of a parallel magnetic field. Reproduced from ref 150. Copyright 2012 American Chemical Society. (E) SEM image of a hexapod. (F, G) SEM images of dried assembled hexapods without (F) and with (G) the magnetic field. (H) Schematic illustration of hexapod rearrangement in the chain upon application of a magnetic field. Reproduced from ref 151. Copyright 2018 American Chemical Society.

magnetic dipole in the hematite, the particles can self-assemble into clusters even without an external magnetic field. The

number of particles in the clusters, either two (Figure 18B) or three (Figure 18C), can be finely controlled by changing the
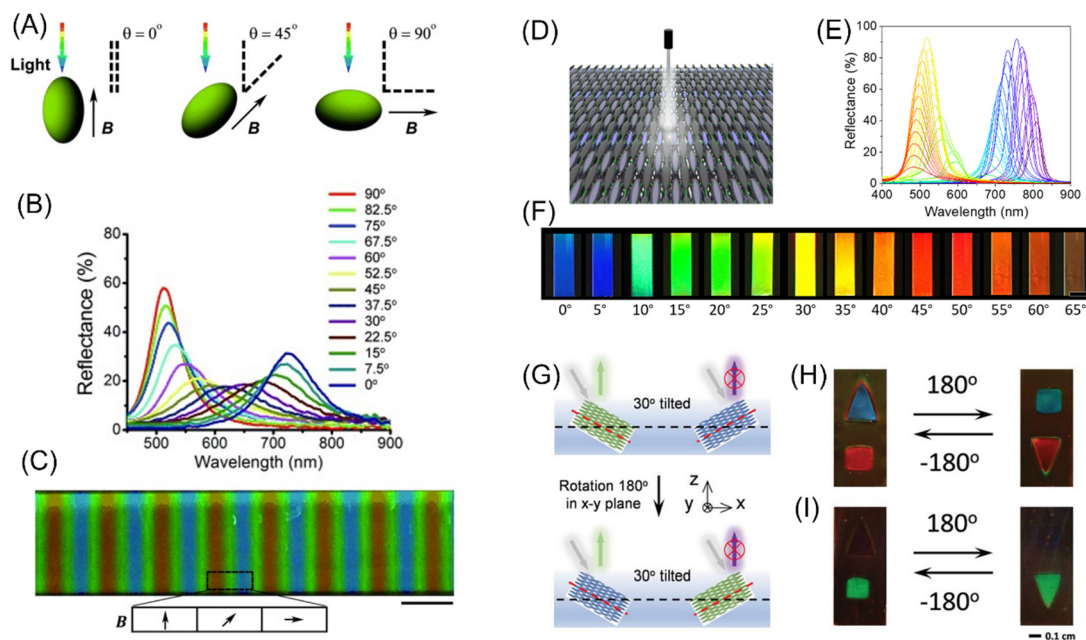
Figure 19. (A) Schematic representation of the spontaneous alignment of nanoellipsoids under magnetic fields. (B) Reflection spectra of photonic structures under magnetic fields with varying directions relative to light incidence. (C) Digital photo showing the photonic response of the nanoellipsoids solution under a linear Halbach array. Scale bar: 5 mm. Reproduced from ref 3. Copyright 2015 Wiley. (D) Schematic illustration of measuring the crystal optical properties. (E, F) Measured reflection spectra (E) and colors (F) of rod dispersion under different magnetic fields. Reproduced from ref 2. Copyright 2021 AAAS. (G) Schematic illustration of the alignment of the photonic pigments in the solid film for mechanochromic responses. (H, I) Digital photos of two photonic films showing color changes in response to rotation (incident angle for H: 30° and I: 40°). Reproduced from ref 171. Copyright 2022 Wiley.

volume of the polymer shell. By applying a magnetic field parallel to the substrate, zigzag chains (Figure 18D) similar to the result of Ge et al. are formed. Kim et al. later found that the SiO_2 rods could be grown on the six faces of the hematite microcubes by the sol−gel reaction, leading to the formation of hexapods, as shown in Figure 18E.[152] The growth mechanism is similar to the Janus rods mentioned above.[148] Jia et al. studied the assembly behavior of these magnetic hexapods under electric and magnetic fields.[151] Under an alternating electric field, the hexapods form linear chains within which the particles are randomly orientated (Figure 18F). At this time, if an additional magnetic field is applied parallel to the substrate, the particles in the chains undergo rotations to correct the misalignment of the magnetic dipoles due to the Zeeman interaction (Figure 18G). After this intermediate disordered state, the particles eventually form linear chains with a higher degree of order than the initial chains.

5. APPLICATIONS

5.1. Photonic Crystals

Photonic crystals are structures with a periodic arrangement of dielectric constants in space. They have received extensive interest in the past few decades because of their ability to create a range of "forbidden" frequencies for light propagation (photonic bandgap).[153,154] Photonic crystals can be produced by microfabrication methods typically involving photolithography, film deposition, and selective etching.[155,156] They can also be formed by self-assembling preformed building blocks (nanoscale objects or block copolymers) into periodic structures,[29,157] offering many advantages such as high efficiency, high speed, cost-effectiveness, and high throughput on large areas.[158]

The self-assembly approaches become more powerful in producing photonic crystals when magnetic particles are employed as the building blocks and magnetic fields to provide the driving force. In addition to creating the desired periodic arrangement, the magnetic field also acts as an efficient stimulus for dynamically tuning the periodicity and, thus, the photonic bandgap.[159] The resulting photonic crystals can exhibit controllable color changes that can respond to or be manipulated by the externally applied magnetic field. They have attracted enormous research interest in the past few decades due to their appealing applications in color displays,[160−163] sensors,[104,164] anticounterfeiting,[165−167] and rewritable signage.[29,103,168]

Compared with isotropic building blocks, one of the important features of anisotropic particles is their shape-dependent physical and chemical properties, which can add more degrees of freedom for manipulating the collective properties of the resultant superstructures.[3] Besides, theoretical calculations have demonstrated that assembling nonspherical nanoparticles holds a greater promise to create photonic crystals with a complete bandgap.[169,170]

Another important feature of photonic crystals made from anisotropy magnetic building blocks is their field direction-dependent optical properties because the orientation of individual particles and the whole superlattice can be magnetically controlled. Wang et al. showed that when the light and the magnetic field are perpendicular, the interplanar spacing is determined by the short axis of nanoellipsoids, resulting in a reflection peak at a shorter wavelength.[3] When they are parallel, the interplanar spacing is determined by the long axis of nanoellipsoids, accounting for a reflection peak at a longer wavelength. Moreover, a continuous blueshift of the reflection peak (from 750 to 500 nm, Figure 19B) is observed
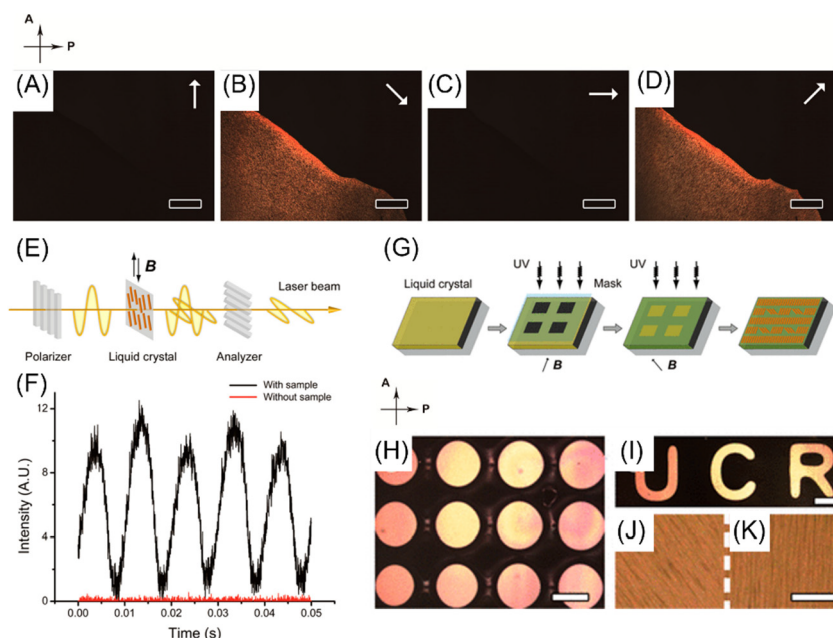
Figure 20. (A–D) Polarized optical microscopy (POM) images of a magnetic liquid crystal film under magnetic fields oriented in different directions. Scale bars: 500 μm. (E) Scheme showing the optical switching test. (F) Transmittance intensity profile of a magnetic liquid crystal under an alternating magnetic field. (G) Scheme showing the lithography process for fabricating thin films with patterns of different polarizations. (H, I) POM images of various polarization-modulated patterns. Scale bars: 500 μm. (J, K) Enlarged OM image shows the arrangement of nanorods in the pattern (J) and surrounding area (K). Scale bar: 10 μm. Reproduced from ref 176. Copyright 2014 American Chemical Society.

when the angle between the magnetic field and light gradually increases from 0° to 90°. Similar field direction-dependent colors have also been reported by Liu et al.[120]

Li et al. demonstrated that with nanoellipsoids of a larger aspect ratio, the assembled photonic crystals showed a much larger tuning range of colors from 480 to 800 nm by increasing the angle between the magnetic field and light from 0° to 65° (Figure 19E and F).[2] More redshift of the reflection peak was observed when the angle was further increased. A rotation-asymmetric mechano-chromic device was fabricated based on these highly tunable multicolor photonic crystals.[171] The film displayed a uniform green color when the ellipsoids were magnetically aligned along 30° to the film surface and illuminated with the incident light at 30°. However, when the film was rotated 180° around its surface normal, the film's color disappeared due to the decrease in incident angle and the consequent blueshift of the diffraction to the UV, exhibiting on–off switching of the structural colors (Figure 19H). When the incident angle was changed to 40°, the color could be switched between red and blue by the same rotation (Figure 19I). Such rotation-asymmetric color change is not achievable by conventional opal or inverse opal photonic crystals made from isotropic building blocks due to their high lattice symmetry.

5.2. Magnetically Actuated Liquid Crystals

Light can change polarization by passing through liquid crystals containing aligned molecules or colloidal nanoparticles of anisotropic shapes. Such a phenomenon is known as birefringence. Due to their application in electronic displays, they have received vast interest since the 1970s.[172] The alignment of liquid crystals can be realized by many external stimuli, such as temperature, flow, and electric and magnetic fields.[173] Compared with the conventional electrically driven liquid crystals, those operating under magnetic fields have the advantages of contactless and remote control, attracting significant interest in the synthesis and fabrication of magnetically actuated liquid crystals.

For the molecule-based liquid crystals, an extremely strong magnetic field ($\sim$1 T) and a long response time are required to align the molecules because of their relatively low magnetic susceptibilities, which severely limit their applications.[174,175] To solve this problem, Wang et al. fabricated the magnetic field-controlled liquid crystals using Fe_3O_4 microrods with a high aspect ratio (length: 1.5 μm, width: 200 nm), which is responsive to a weak magnetic field ($\sim$1 mT).[176] The intensity of transmitted light can be dynamically controlled by magnetic field direction, as shown in Figure 20A–D, which is intrinsically originated from the refractive indices difference between the longitudinal and transverse directions of the Fe_3O_4 microrods. Similar liquid-crystal-like behavior cannot be realized using the assembled structures from magnetic nanospheres. This liquid crystal was extremely sensitive to the directional change of external magnetic fields and exhibited an instant response to an alternating magnetic field of 5 mT within 0.01 s (Figure 20F), corresponding to a switching frequency of 100 Hz, which is comparable to the performance of commercial liquid crystals based on electrical switching. The fast response is inherent from the strong Zeeman interaction between the large dipole moment of the microrod and the external magnetic field: only a moderate field strength is required to generate enough force to overcome the Brownian motion and rotate the microrods. Another advantage of such liquid crystals is the convenience of fabricating complex patterns by combining magnetic alignment and lithography processes (Figure 20G). Regions with different alignments of rods are fixed step-wisely upon exposure to UV light with the aid of UV polymerizable resin and a photomask. The as-made films showed distinct contrast under polarized optical microscopy. Similar iron oxide nanoparticles based magneti-
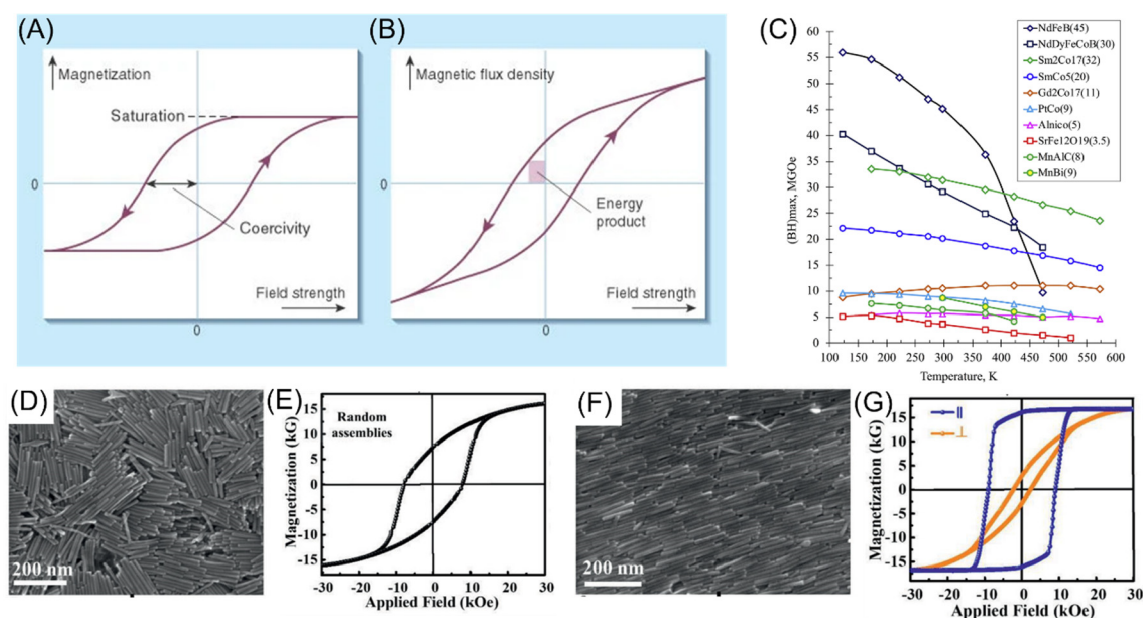
Figure 21. (A, B) Response of a magnet to an applied field in terms of its magnetization (A) and the magnetic induction or flux density (B). Reproduced from ref 179. Copyright 2002 Nature Publishing Group. (C) Temperature dependence of maximum energy products for most commercial permanent magnets. Reproduced from ref 177. Copyright 2018 Elsevier. (D, E) SEM images of randomly oriented (D) and unidirectional oriented (E) Co nanowire assembly. (F, G) Magnetization loop of randomly oriented NWs (F) and unidirectional oriented (G) Co nanowires at 300 K. Reproduced from ref 187. Copyright 2021 Wiley.

cally responsive liquid crystals have also been reported in others' works.[120,144,171]

5.3. Rare-Earth-Free Permanent Magnets with High-Energy Product

Permanent magnets are critical components in the traction motor of electric vehicles and the power generator of wind turbines.[177] The rapid development of renewable and clean energy promotes an increasing demand for the supply of high-performance permanent magnets in the foreseeable future. The maximum energy product measures the maximum amount of magnetic energy stored in a magnet and is used as an indicator of magnet strength.[178] Current permanent magnets having high energy products are all based on rare-earth compounds (energy product ~50 MGOe,[179] 1 MGOe = 7.958 kJ m^{-3}) that have extraordinarily high magneto-crystalline anisotropy provided by the rare-earth 4f electrons.[180] However, rare-earth compound-based permanent magnets suffer from some disadvantages. For example, their thermal stability is relatively poor (Curie temperature = 310−400 °C) compared to ferromagnetic 3d transition metals like Fe, Co, and their alloys (Curie temperature > 700 °C), hindering their applications that require high temperatures. Besides, their future supply has remained a concern due to the scarcity of rare-earth elements in the earth's crust.[181] Thus, there is a significant demand for producing rare-earth-free permanent magnets with a high energy product.[177,182]

A large energy product requires a large saturation magnetization and a large coercivity, as shown in Figure 21A. Although they have a higher saturation magnetization and Curie temperatures, the 3d elements and their alloys, known as "soft magnetic materials," have a low coercivity and energy product due to their low magneto-crystalline anisotropy. Therefore, improving the coercivity of soft magnetic materials has been a hot research topic over the years.[183−186]

Recent research has shown that the coercivity can be greatly enhanced by self-assembling the magnetic nanorods into ordered structures (Figure 21D−G). In 2014, Fang et al. reported that aligned single-crystalline Co nanorods could have a coercivity of up to 7.0 kOe at room temperature.[13] Around the same time, Gandha et al. reported that the magnetic alignment of single-crystalline Co nanorods with diameters of 15 nm and an average length of 200 nm could produce a high coercivity of 10.6 kOe and an energy product of 44 MGOe at room temperature.[188] The uniformity of nanorod morphology was also found to play an important role in determining the coercivity and magnetization hysteresis. Anagnostopoulou et al. systematically investigated the influence of rod diameter, magnetic volume fraction, and assembly method on the energy product of assembled Co nanorods.[189] The highest energy product was obtained from nanorods with a smaller diameter and higher magnetic volume fraction (with less surface oxidation). A better order with fewer defects also positively contributed to the energy product. The high value of coercivity of assembled Co nanorods is benefited from the coupling between the shape anisotropy and high magneto-crystalline anisotropy of Co.[190]

Despite the significantly enhanced energy product values of assembled Co nanorods under room temperature (300 K), the discussion of their performance under elevated temperature is rare. A literature report indicates that only ~50% of the room temperature coercivity is preserved at 500 K for assembled Co nanorods.[191] Although this value is better than that of the NdFeB magnet, further optimization is still needed.

5.4. Mechanical Enhancement Materials

Materials with excellent mechanical properties, including large bonding strength, high elastic modulus, and large hardness, have been long desired. Traditional metals and ceramics are usually damage-intolerant since their performances are severely limited by the damage-induced defects inside.
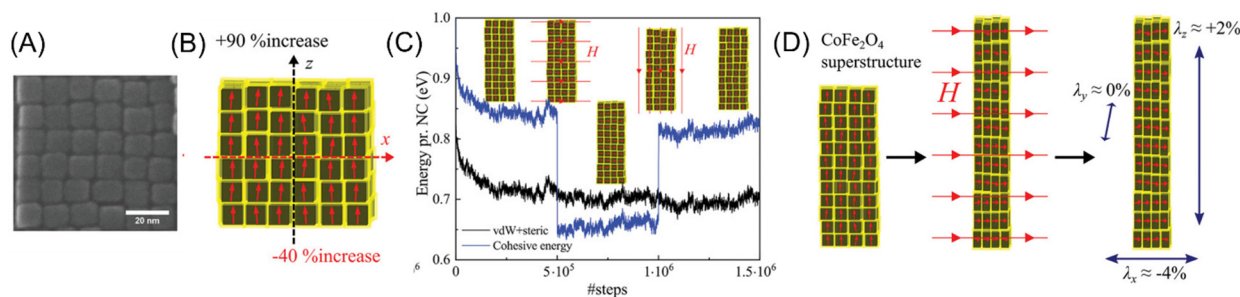
Figure 22. (A) SEM images of cobalt ferrite superstructure with vertically aligned macrospins. (B) Mechanical anisotropy of the superstructure. (C) Reconfigurability of mechanical properties via applied magnetic fields. (D) Reconfigurable supermagnetostriction of cobalt ferrite superstructures. Reproduced from ref 128. Copyright 2021 Wiley.

Additionally, the high processing temperature of these materials consumes a large portion of energy. Organic—inorganic mesocrystals are hybrid materials consisting of crystalline inorganic nanoparticles and interspacing amorphous organic layers. This structure combines disparate materials, such as hard but brittle nanocrystals, with a soft and ductile amorphous material, enabling a mechanically optimized structural design.[192] Many living organisms adopt this strategy to produce mechanically outstanding materials by combining minerals with biopolymers. For example, a mollusk shell or nacre is composed of hard calcium carbonate minerals and soft organics, yielding a high strength and impressive fracture toughness about 3000 times higher than the minerals.[193]

Recently, Hakonsen et al. theoretically investigated the influence of magnetic interactions on the mechanical properties of the assembled superstructure of magnetic nanocubes.[128] Van der Waals interaction, steric repulsion, and magnetic dipole—dipole interactions are considered when calculating the cohesive energy (the energy required to break the assembled structures up into isolated building blocks) of the assembled structures using the Monte Carlo simulation method. For $CoFe_2O_4$ nanocubes, which possess a high magneto-crystalline anisotropy constant along its [100] crystallographic axes, their magnetic dipoles do not undergo a relaxation process and remain unidirectionally aligned even when the external field is removed. These directionally "blocked" magnetic dipoles lead to an anisotropic mechanical enhancement of the superstructure, with a 90% increase along the dipole direction and an ∼40% decrease along the other two directions (Figure 22B). Such a directional mechanical enhancement is also shape-dependent. The enhancement is more dramatic along the long axis of the stripe-shaped superstructures. The interesting aspect of this structure is the possibility of magnetic field control of the mechanical anisotropy through changes in the permanent magnetization direction. Another property of the assembled superstructure in Figure 22D is the enhanced magnetostriction, which is at least 1 order of magnitude larger than that of conventional materials (Terfenol-D). Moreover, this supermagnetostriction can also be controlled by the direction of applied magnetic fields. With these novel properties, this superstructure may find applications such as sensors based on microelectromechanical systems (MEMS), scaffolds for tissue engineering, and bioinspired artificial materials with field-controlled reconfigurable mechanical properties.

6. SUMMARY AND OUTLOOK

Distinct from spherical nanoparticles, the self-assembly of nanoparticles with anisotropic shapes has been an active research topic for a long time. However, their orientational control on demand is often problematic not only in the solution but also during the assembly process. For magnetic nanoparticles, the interaction between the induced magnetic dipole and the external magnetic field provides a convenient method to dynamically control their orientation. The overall magnetization direction of colloidal nanoparticles is determined by their magnetic anisotropy, which is influenced by many factors such as crystal phase, particle shape, and crystal microstructure. Thus, understanding the magnetic anisotropy of a nonspherical particle is imperative to predict how it behaves and how it interacts with neighbors under the external magnetic field. This Review summarizes the preparation of magnetic nanoparticles with anisotropic shapes, including rods, cubes, plates, peanuts, and hybrid particles. For each shape, the magnetic anisotropy is analyzed based on the magneto-crystalline and shape anisotropy. This unique magnetic anisotropy enables the dynamic orientational control of the magnetic nanoparticles in the solution by simply changing the direction of the magnetic field. It also makes it possible to assemble them into superstructures with long-range orientational and positional orders using magnetic fields. Although the past decade has witnessed rapid growth in the preparation of uniform nonspherical magnetic nanoparticles and assembled superstructures from these building blocks, there are still plenty of opportunities for further development. Here we point out the following aspects:

(1) Complex systems involving nanoparticles with two different sizes or shapes (i.e., binary superlattices) have been investigated for nonmagnetic and spherical magnetic nanoparticles.[194−198] However, current research on the self-assembly of anisotropic magnetic nanoparticles still focuses on particles of uniform shape and magnetic anisotropy, largely because of the limited understanding of and control over the magnetic properties of the synthesized nanoparticles. Complex assembly behaviors will emerge if two types of magnetic nanoparticles are present in the same solution, for example, magnetic nanorods with the same morphology but different easy magnetization directions. The coassembly of these nanoparticles with different types of magnetic anisotropy is expected to produce novel superlattices that are not attainable in conventional assembly methods, opening the door to understanding the fundamental aspects of nanoscale magnetic assembly and simultaneously providing a robust platform to build new functional materials.

(2) Iron oxide nanoparticles have been widely used as active materials in biomedicine, such as drug carriers,[199−201] hyperthermia agents,[202−205] and contrast agents in magnetic resonance imaging,[206−208] due to their low cytotoxicity and unique physical properties. It was found that iron oxide nanoparticles with anisotropic morphologies have better performance than their spherical counterparts for hyperthermia.[209] Meanwhile, it is also found that the magnetic chains obtained from the assembly of nanospheres show a directional heating effect under an ac magnetic field.[210] These interesting phenomena suggest that assembling magnetic nanoparticles into superstructures is promising to promote their performance in biological applications, and their collective properties are highly dependent on the symmetry and size of the superstructures. Nevertheless, more efforts are still required to understand how the magnetic anisotropy and the resulting superstructures affect the collective physical properties. The improved understanding will enable the use of anisotropic magnetic nanoparticles for the rational design of superstructures with significantly improved performance in biomedical applications.

(3) Magnetic materials represent only a tiny fraction of the library of functional materials. A wide range of nonmagnetic nanostructures possess special optical, electrical, mechanical, and catalytic properties and are, therefore, better candidates for achieving specific functionalities. When made into anisotropic shapes, such nonmagnetic nanostructures often exhibit unique and orientation-dependent physical properties compared to their spherical counterparts, such as localized surface plasma resonance[211−216] and polarized light emission.[217−219] However, fully exploiting their shape-dependent properties is hampered by the lack of efficient assembly strategies to realize positional and orientational control. As such, incorporating magnetic components into these anisotropic nanostructures is a powerful solution to this challenge, conferring the advantages of the magnetic assembly strategy,[30,220−223] including convenience, flexibility, efficiency, remote control, and scalability. It is worth pointing out that, in some cases, the magnetic components may interfere with the desired properties and therefore need to be removed after the assembly process.

(4) Most current magnetic assembly approaches involve uniform static magnetic fields to take advantage of their defined field strength and direction. Many prior works have fully demonstrated the associated benefits in enabling long-range order in the formed superstructures and precise control over the orientational and positional order on a large scale. Field gradient is another important parameter of a magnetic field, but its impact on the nanoscale magnetic assembly has not been systematically studied. Anisotropic magnetic nanostructures are expected to adopt the spatial distribution of a gradient magnetic field and produce gradient orientational and population distribution. It will be interesting to explore how the field gradient can be utilized to design superstructures whose symmetry and properties are not uniform but fit the special functionalities desired for the target applications. In addition, it is also important to study the magnetic interactions of the anisotropic nanostructures and their assembly behaviors under rotating or alternating magnetic fields.[224−226] Many challenges are anticipated as new tools and methods are needed to properly characterize the assembly behaviors in these different types of magnetic fields, but new opportunities are also expected to further improve our fundamental understanding of nanoscale magnetic assembly and create new functionalities to better serve practical applications.

AUTHOR INFORMATION

Corresponding Author

Yadong Yin − *Department of Chemistry, University of California, Riverside, California 92521, United States;* orcid.org/0000-0003-0218-3042; Email: yadongy@ucr.edu

Authors

Qingsong Fan − *Department of Chemistry, University of California, Riverside, California 92521, United States*
Zhiwei Li − *Department of Chemistry, University of California, Riverside, California 92521, United States*
Chaolumen Wu − *Department of Chemistry, University of California, Riverside, California 92521, United States*

Complete contact information is available at:
https://pubs.acs.org/10.1021/prechem.3c00012

Notes

The authors declare no competing financial interest.

REFERENCES

(1) Ding, T.; Song, K.; Clays, K.; Tung, C.-H. Fabrication of 3D Photonic Crystals of Ellipsoids: Convective Self-Assembly in Magnetic Field. *Adv. Mater.* **2009**, *21* (19), 1936−1940.

(2) Li, Z.; Qian, C.; Xu, W.; Zhu, C.; Yin, Y. Coupling morphological and magnetic anisotropy for assembling tetragonal colloidal crystals. *Sci. Adv.* **2021**, *7* (37), No. eabh1289.

(3) Wang, M.; He, L.; Xu, W.; Wang, X.; Yin, Y. Magnetic assembly and field-tuning of ellipsoidal-nanoparticle-based colloidal photonic crystals. *Angew. Chem., Int. Ed.* **2015**, *54* (24), 7077−7081.

(4) Shi, L.; Zhu, L.; Guo, J.; Zhang, L.; Shi, Y.; Zhang, Y.; Hou, K.; Zheng, Y.; Zhu, Y.; Lv, J.; Liu, S.; Tang, Z. Self-Assembly of Chiral Gold Clusters into Crystalline Nanocubes of Exceptional Optical Activity. *Angew. Chem., Int. Ed.* **2017**, *56* (48), 15397−15401.

(5) Zhang, X.; Li, Z.; Feng, J.; Yang, F.; Wu, C.; Fan, Q.; Zhou, S.; Yin, Y. Dynamic Tuning of Optical Transmittance of 1D Colloidal Assemblies of Magnetic Nanostructures. *Adv. Intell. Syst.* **2019**, *1* (8), 1900099.

(6) Bian, K.; Schunk, H.; Ye, D.; Hwang, A.; Luk, T. S.; Li, R.; Wang, Z.; Fan, H. Formation of self-assembled gold nanoparticle supercrystals with facet-dependent surface plasmonic coupling. *Nat. Commun.* **2018**, *9* (1), 2365.

(7) Qiao, X.; Su, B.; Liu, C.; Song, Q.; Luo, D.; Mo, G.; Wang, T. Selective Surface Enhanced Raman Scattering for Quantitative Detection of Lung Cancer Biomarkers in Superparticle@MOF Structure. *Adv. Mater.* **2018**, *30* (5), 1702275.

(8) Mayer, M.; Schnepf, M. J.; König, T. A. F.; Fery, A. Colloidal Self-Assembly Concepts for Plasmonic Metasurfaces. *Adv. Opt. Mater.* **2019**, *7* (1), 1800564.

(9) Li, Z.; Wang, W.; Yin, Y. Colloidal Assembly and Active Tuning of Coupled Plasmonic Nanospheres. *Trends in Chemistry* **2020**, *2* (7), 593−608.

(10) Huang, C.; Dong, J.; Sun, W.; Xue, Z.; Ma, J.; Zheng, L.; Liu, C.; Li, X.; Zhou, K.; Qiao, X.; Song, Q.; Ma, W.; Zhang, L.; Lin, Z.; Wang, T. Coordination mode engineering in stacked-nanosheet metal-organic frameworks to enhance catalytic reactivity and structural robustness. *Nat. Commun.* **2019**, *10* (1), 2779.

(11) Xu, G.; Liu, J.; Liu, B.; Zhang, J. Self-assembly of Pt nanocrystals into three-dimensional superlattices results in enhanced electrocatalytic performance for methanol oxidation. *CrystEngComm* **2019**, *21* (3), 411−419.

(12) Urban, J. J.; Talapin, D. V.; Shevchenko, E. V.; Kagan, C. R.; Murray, C. B. Synergism in binary nanocrystal superlattices leads to enhanced p-type conductivity in self-assembled PbTe/Ag2 Te thin films. *Nat. Mater.* **2007**, *6* (2), 115−121.

(13) Fang, W.; Panagiotopoulos, I.; Ott, F.; Boué, F.; Ait-Atmane, K.; Piquemal, J.-Y.; Viau, G.; Dalmas, F. Optimization of the magnetic properties of aligned Co nanowires/polymer composites for the fabrication of permanent magnets. *J. Nanoparticle Res.* **2014**, *16* (2), 1−10.

(14) Lalatonne, Y.; Motte, L.; Russier, V.; Ngo, A.; Bonville, P.; Pileni, M. Mesoscopic structures of nanocrystals: collective magnetic properties due to the alignment of nanocrystals. *J. Phys. Chem. B* **2004**, *108* (6), 1848−1854.

(15) Dreyer, A.; Feld, A.; Kornowski, A.; Yilmaz, E. D.; Noei, H.; Meyer, A.; Krekeler, T.; Jiao, C.; Stierle, A.; Abetz, V.; Weller, H.; Schneider, G. A. Organically linked iron oxide nanoparticle super-crystals with exceptional isotropic mechanical properties. *Nat. Mater.* **2016**, *15* (5), 522−528.

(16) Gu, X. W.; Ye, X.; Koshy, D. M.; Vachhani, S.; Hosemann, P.; Alivisatos, A. P. Tolerance to structural disorder and tunable mechanical behavior in self-assembled superlattices of polymer-grafted nanocrystals. *Proc. Natl. Acad. Sci. U.S.A.* **2017**, *114* (11), 2836−2841.

(17) Mueggenburg, K. E.; Lin, X. M.; Goldsmith, R. H.; Jaeger, H. M. Elastic membranes of close-packed nanoparticle arrays. *Nat. Mater.* **2007**, *6* (9), 656−660.

(18) Xu, W.; Li, Z.; Yin, Y. Colloidal assembly approaches to micro/nanostructures of complex morphologies. *Small* **2018**, *14* (35), 1801083.

(19) Li, Z.; Fan, Q.; Yin, Y. Colloidal Self-Assembly Approaches to Smart Nanostructured Materials. *Chem. Rev.* **2022**, *122* (5), 4976−5067.

(20) Grzelczak, M.; Vermant, J.; Furst, E. M.; Liz-Marzán, L. M. Directed self-assembly of nanoparticles. *ACS Nano* **2010**, *4* (7), 3591−3605.

(21) Xia, Y.; Gates, B.; Yin, Y.; Lu, Y. Monodispersed colloidal spheres: old materials with new applications. *Adv. Mater.* **2000**, *12* (10), 693−713.

(22) Xia, Y.; Yin, Y.; Lu, Y.; McLellan, J. Template-Assisted Self-Assembly of Spherical Colloids into Complex and Controllable Structures. *Adv. Funct. Mater.* **2003**, *13* (12), 907−918.

(23) Zhang, J.; Li, Y.; Zhang, X.; Yang, B. Colloidal self-assembly meets nanofabrication: from two-dimensional colloidal crystals to nanostructure arrays. *Adv. Mater.* **2010**, *22* (38), 4249−4269.

(24) Boles, M. A.; Engel, M.; Talapin, D. V. Self-Assembly of Colloidal Nanocrystals: From Intricate Structures to Functional Materials. *Chem. Rev.* **2016**, *116* (18), 11220−11289.

(25) Lotito, V.; Zambelli, T. Approaches to self-assembly of colloidal monolayers: A guide for nanotechnologists. *Adv. Colloid Interface Sci.* **2017**, *246*, 217−274.

(26) William, L. *Fundamentals of geophysics*; Cambridge University Press: 2007.

(27) Wang, M.; He, L.; Yin, Y. Magnetic field guided colloidal assembly. *Mater. Today* **2013**, *16* (4), 110−116.

(28) Kraftmakher, Y. Magnetic field of a dipole and the dipole−dipole interaction. *Eur. J. Phys.* **2007**, *28* (3), 409−414.

(29) Ge, J.; Yin, Y. Responsive photonic crystals. *Angew. Chem., Int. Ed.* **2011**, *50* (7), 1492−1522.

(30) Wang, M.; Gao, C.; He, L.; Lu, Q.; Zhang, J.; Tang, C.; Zorba, S.; Yin, Y. Magnetic tuning of plasmonic excitation of gold nanorods. *J. Am. Chem. Soc.* **2013**, *135* (41), 15302−15305.

(31) Tseng, P.; Lin, J.; Owsley, K.; Kong, J.; Kunze, A.; Murray, C.; Di Carlo, D. Flexible and stretchable micromagnet arrays for tunable biointerfacing. *Adv. Mater.* **2015**, *27* (6), 1083−1089.

(32) Coey, J. M. *Magnetism and magnetic materials*; Cambridge University Press: 2010.

(33) Tronc, E. Magnetic relaxation in fine-particle systems. *Adv. Chem. Phys.* **2007**, *283*, 283−449.

(34) Kittel, C. Physical Theory of Ferromagnetic Domains. *Rev. Mod. Phys.* **1949**, *21* (4), 541−583.

(35) Prigogine, I.; Rice, S. A. *Advances in chemical physics*; John Wiley & Sons: 2009; Vol. *218*.

(36) Skomski, R.; Manchanda, P.; Kashyap, A., Anisotropy and Crystal Field. In *Handbook of Magnetism and Magnetic Materials*; Springer: 2021; pp 1−83.

(37) Snoeck, E.; Gatel, C.; Lacroix, L.-M.; Blon, T.; Lachaize, S.; Carrey, J.; Respaud, M.; Chaudret, B. Magnetic configurations of 30 nm iron nanocubes studied by electron holography. *Nano Lett.* **2008**, *8* (12), 4293−4298.

(38) Shavel, A.; Rodríguez-González, B.; Spasova, M.; Farle, M.; Liz-Marzán, L. M. Synthesis and Characterization of Iron/Iron Oxide Core/Shell Nanocubes. *Adv. Funct. Mater.* **2007**, *17* (18), 3870−3876.

(39) Park, J.; An, K.; Hwang, Y.; Park, J. G.; Noh, H. J.; Kim, J. Y.; Park, J. H.; Hwang, N. M.; Hyeon, T. Ultra-large-scale syntheses of monodisperse nanocrystals. *Nat. Mater.* **2004**, *3* (12), 891−895.

(40) Margeat, O.; Dumestre, F.; Amiens, C.; Chaudret, B.; Lecante, P.; Respaud, M. Synthesis of iron nanoparticles: Size effects, shape control and organisation. *Prog. Solid State Chem.* **2005**, *33* (2−4), 71−79.

(41) Skomski, R. Nanomagnetics. *J. Condens. Matter Phys.* **2003**, *15* (20), R841.

(42) LaGrow, A. P.; Ingham, B.; Cheong, S.; Williams, G. V.; Dotzler, C.; Toney, M. F.; Jefferson, D. A.; Corbos, E. C.; Bishop, P. T.; Cookson, J.; Tilley, R. D. Synthesis, alignment, and magnetic properties of monodisperse nickel nanocubes. *J. Am. Chem. Soc.* **2012**, *134* (2), 855−858.

(43) Xiao, L.; Zhou, T.; Chen, Y.; Wang, Z.; Zheng, H.; Xu, W.; Zeng, D.; Peng, D.-L. Tungsten hexacarbonyl-induced growth of nickel nanorods and nanocubes. *Mater. Lett.* **2018**, *229*, 340−343.

(44) Donegan, K. P.; Godsell, J. F.; Tobin, J. M.; O'Byrne, J. P.; Otway, D. J.; Morris, M. A.; Roy, S.; Holmes, J. D. Microwave-assisted synthesis of icosahedral nickel nanocrystals. *CrystEngComm* **2011**, *13* (6), 2023−2028.

(45) Kim, C.; Kim, C.; Lee, K.; Lee, H. Shaped Ni nanoparticles with an unconventional hcp crystalline structure. *Chem. Commun. (Camb)* **2014**, *50* (48), 6353−6356.

(46) Puntes, V. F.; Zanchet, D.; Erdonmez, C. K.; Alivisatos, A. P. Synthesis of hcp-Co nanodisks. *J. Am. Chem. Soc.* **2002**, *124* (43), 12874−12880.

(47) Dumestre, F.; Chaudret, B.; Amiens, C.; Fromen, M.-C.; Casanove, M.-J.; Renaud, P.; Zurcher, P. Shape Control of Thermodynamically Stable Cobalt Nanorods through Organometallic Chemistry. *Angew. Chem., Int. Ed.* **2002**, *41* (22), 4286−4289.

(48) Dumestre, F.; Chaudret, B.; Amiens, C.; Respaud, M.; Fejes, P.; Renaud, P.; Zurcher, P. Unprecedented Crystalline Super-Lattices of Monodisperse Cobalt Nanorods. *Angew. Chem., Int. Ed.* **2003**, *115*, 5213−5216.

(49) Meziane, L.; Salzemann, C.; Aubert, C.; Gerard, H.; Petit, C.; Petit, M. Hcp cobalt nanocrystals with high magnetic anisotropy prepared by easy one-pot synthesis. *Nanoscale* **2016**, *8* (44), 18640−18645.

(50) Shukla, N.; Liu, C.; Roy, A. G. Oriented self-assembly of cubic FePt nanoparticles. *Mater. Lett.* **2006**, *60* (8), 995−998.

(51) Chen, M.; Kim, J.; Liu, J.; Fan, H.; Sun, S. Synthesis of FePt nanocubes and their oriented self-assembly. *J. Am. Chem. Soc.* **2006**, *128* (22), 7132−7133.

(52) Chou, S.-W.; Zhu, C.-L.; Neeleshwar, S.; Chen, C.-L.; Chen, Y.-Y.; Chen, C.-C. Controlled Growth and Magnetic Property of FePt Nanostructure: Cuboctahedron, Octapod, Truncated Cube, and Cube. *Chem. Mater.* **2009**, *21* (20), 4955−4961.

(53) Yuan, J.; Li, C.-F.; Liu, Z.-Q.; Wu, D.; Cao, L. Synthesis of variously shaped magnetic FeCo nanoparticles and the growth mechanism of FeCo nanocubes. *CrystEngComm* **2017**, *19* (43), 6506−6515.

(54) Wei, X. W.; Zhu, G. X.; Liu, Y. J.; Ni, Y. H.; Song, Y.; Xu, Z. Large-Scale Controlled Synthesis of FeCo Nanocubes and Microcages by Wet Chemistry. *Chem. Mater.* **2008**, *20* (19), 6248−6253.

(55) Roberts, A. P.; Zhao, X.; Hu, P.; Abrajevitch, A.; Chen, Y. H.; Harrison, R. J.; Heslop, D.; Jiang, Z.; Li, J.; Liu, Q.; Muxworthy, A. R.; Oda, H.; O'Neill, H. S. C.; Pillans, B. J.; Sato, T. Magnetic Domain State and Anisotropy in Hematite (α-Fe2O3) From First-Order Reversal Curve Diagrams. *J. Geophys. Res. Solid Earth* **2021**, *126* (12), No. e2021JB023027.

(56) Meijer, J.-M.; Byelov, D. V.; Rossi, L.; Snigirev, A.; Snigireva, I.; Philipse, A. P.; Petukhov, A. V. Self-assembly of colloidal hematite cubes: a microradian X-ray diffraction exploration of sedimentary crystals. *Soft Matter* **2013**, *9* (45), 10729−10738.

(57) Ni, Y.; Ge, X.; Zhang, Z.; Ye, Q. Fabrication and characterization of the plate-shaped γ-Fe2O3 nanocrystals. *Chem. Mater.* **2002**, *14* (3), 1048−1052.

(58) Lu, J.; Jiao, X.; Chen, D.; Li, W. Solvothermal synthesis and characterization of Fe3O4 and γ-Fe2O3 nanoplates. *J. Phys. Chem. C* **2009**, *113* (10), 4012−4017.

(59) Muro-Cruces, J.; Roca, A. G.; Lopez-Ortega, A.; Fantechi, E.; Del-Pozo-Bueno, D.; Estrade, S.; Peiro, F.; Sepulveda, B.; Pineider, F.; Sangregorio, C.; Nogues, J. Precise Size Control of the Growth of Fe3O4 Nanocubes over a Wide Size Range Using a Rationally Designed One-Pot Synthesis. *ACS Nano* **2019**, *13* (7), 7716−7728.

(60) Yang, H.; Ogawa, T.; Hasegawa, D.; Takahashi, M. Synthesis and magnetic properties of monodisperse magnetite nanocubes. *J. Appl. Phys.* **2008**, *103* (7), 07d526.

(61) Gao, G.; Liu, X.; Shi, R.; Zhou, K.; Shi, Y.; Ma, R.; Takayama-Muromachi, E.; Qiu, G. Shape-Controlled Synthesis and Magnetic Properties of Monodisperse Fe3O4 Nanocubes. *Cryst. Growth Des.* **2010**, *10* (7), 2888−2894.

(62) Song, Q.; Zhang, Z. J. Controlled synthesis and magnetic properties of bimagnetic spinel ferrite CoFe2O4 and MnFe2O4 nanocrystals with core-shell architecture. *J. Am. Chem. Soc.* **2012**, *134* (24), 10182−10190.

(63) Vestal, C. R.; Song, Q.; Zhang, Z. J. Effects of Interparticle Interactions upon the Magnetic Properties of CoFe2O4 and MnFe2O4 Nanocrystals. *J. Phys. Chem. B* **2004**, *108* (47), 18222−18227.

(64) Bao, N.; Shen, L.; An, W.; Padhan, P.; Heath Turner, C.; Gupta, A. Formation Mechanism and Shape Control of Monodisperse Magnetic CoFe2O4 Nanocrystals. *Chem. Mater.* **2009**, *21* (14), 3458−3468.

(65) Vereda, F.; de Vicente, J.; Hidalgo-Alvarez, R. Physical properties of elongated magnetic particles: magnetization and friction coefficient anisotropies. *ChemPhysChem* **2009**, *10* (8), 1165−1179.

(66) Bedanta, S.; Kleemann, W. Supermagnetism. *J. Phys. D* **2009**, *42* (1), 013001.

(67) Farle, M. Ferromagnetic resonance of ultrathin metallic layers. *Rep. Prog. Phys.* **1998**, *61* (7), 755.

(68) Krahne, R.; Manna, L.; Morello, G.; Figuerola, A.; George, C.; Deka, S. Magnetic Properties of Nanorods. In *Physical Properties of Nanorods*; Springer: 2013; pp 133−213.

(69) Dumestre, F.; Chaudret, B.; Amiens, C.; Fromen, M. C.; Casanove, M. J.; Renaud, P.; Zurcher, P. Shape control of thermodynamically stable cobalt nanorods through organometallic chemistry. *Angew. Chem., Int. Ed.* **2002**, *41* (22), 4286−4289.

(70) Lisjak, D.; Mertelj, A. Anisotropic magnetic nanoparticles: A review of their properties, syntheses and potential applications. *Prog. Mater. Sci.* **2018**, *95*, 286−328.

(71) Labarta, A.; Batlle, X.; Iglesias, O. From finite size and surface effects to glassy behaviour in ferrimagnetic nanoparticles. In *Surface Effects in Magnetic Nanoparticles*; Springer: 2005; pp 105−140.

(72) Callen, E. Magnetostriction. *J. Appl. Phys.* **1968**, *39* (2), 519−527.

(73) Lee, E. W. Magnetostriction and magnetomechanical effects. *Rep. Prog. Phys.* **1955**, *18* (1), 184.

(74) Kwun, H.; Burkhardt, G. L. Effects of grain size, hardness, and stress on the magnetic hysteresis loops of ferromagnetic steels. *J. Appl. Phys.* **1987**, *61* (4), 1576−1579.

(75) Sipeky, A.; Ivanyi, A. Magnetic hysteresis under applied stress. *Phys. B: Condens. Matter* **2006**, *372* (1−2), 177−180.

(76) Hubert, A.; Schäfer, R. *Magnetic domains: the analysis of magnetic microstructures*. Springer Science & Business Media: 2008.

(77) Aharoni, A. *Introduction to the Theory of Ferromagnetism*; Clarendon Press: 2000; Vol. 109.

(78) Soshin, C. *Physics of ferromagnetism*, 2nd ed.; Oxford Science Publication: 2009.

(79) Ruderman, M. A.; Kittel, C. Indirect Exchange Coupling of Nuclear Magnetic Moments by Conduction Electrons. *Phys. Rev.* **1954**, *96* (1), 99−102.

(80) Yosida, K. Magnetic Properties of Cu-Mn Alloys. *Phys. Rev.* **1957**, *106* (5), 893−898.

(81) Nogués, J.; Schuller, I. K. Exchange bias. *J. Magn. Magn. Mater.* **1999**, *192* (2), 203−232.

(82) Kiwi, M. Exchange bias theory. *J. Magn. Magn. Mater.* **2001**, *234* (3), 584−595.

(83) Nogués, J.; Sort, J.; Langlais, V.; Skumryev, V.; Suriñach, S.; Muñoz, J. S.; Baró, M. D. Exchange bias in nanostructures. *Phys. Rep.* **2005**, *422* (3), 65−117.

(84) Xue, X.; Wang, J.; Furlani, E. P. Self-Assembly of Crystalline Structures of Magnetic Core-Shell Nanoparticles for Fabrication of Nanostructured Materials. *ACS Appl. Mater. Interfaces* **2015**, *7* (40), 22515−22524.

(85) Bharti, B.; Kogler, F.; Hall, C. K.; Klapp, S. H.; Velev, O. D. Multidirectional colloidal assembly in concurrent electric and magnetic fields. *Soft Matter* **2016**, *12* (37), 7747−7758.

(86) He, L.; Wang, M.; Ge, J.; Yin, Y. Magnetic assembly route to colloidal responsive photonic nanostructures. *Acc. Chem. Res.* **2012**, *45* (9), 1431−1440.

(87) Singh, G.; Chan, H.; Udayabhaskararao, T.; Gelman, E.; Peddis, D.; Baskin, A.; Leitus, G.; Kral, P.; Klajn, R. Magnetic field-induced self-assembly of iron oxide nanocubes. *Faraday Discuss.* **2015**, *181*, 403−421.

(88) Donaldson, J. G.; Kantorovich, S. S. Directional self-assembly of permanently magnetised nanocubes in quasi two dimensional layers. *Nanoscale* **2015**, *7* (7), 3217−3228.

(89) Håkonsen, V.; Singh, G.; Normile, P. S.; De Toro, J. A.; Wahlström, E.; He, J.; Zhang, Z. Magnetically Enhanced Mechanical Stability and Super-Size Effects in Self-Assembled Superstructures of Nanocubes. *Adv. Funct. Mater.* **2019**, *29* (46), 1904825.

(90) Zhang, X.; Zhang, Z.; Glotzer, S. C. Simulation study of dipole-induced self-assembly of nanocubes. *J. Phys. Chem. C* **2007**, *111* (11), 4132−4137.

(91) Alvarez, C. E.; Klapp, S. H. L. Percolation and orientational ordering in systems of magnetic nanorods. *Soft Matter* **2012**, *8* (28), 7480−7489.

(92) Li, Z.; Yang, F.; Yin, Y. Smart Materials by Nanoscale Magnetic Assembly. *Adv. Funct. Mater.* **2020**, *30* (2), 1903467.

(93) Li, Z.; Wang, M.; Zhang, X.; Wang, D.; Xu, W.; Yin, Y. Magnetic Assembly of Nanocubes for Orientation-Dependent Photonic Responses. *Nano Lett.* **2019**, *19* (9), 6673−6680.

(94) Smoukov, S. K.; Gangwal, S.; Marquez, M.; Velev, O. D. Reconfigurable responsive structures assembled from magnetic Janus particles. *Soft Matter* **2009**, *5* (6), 1285−1292.

(95) Ge, J.; Hu, Y.; Biasini, M.; Beyermann, W. P.; Yin, Y. Superparamagnetic magnetite colloidal nanocrystal clusters. *Angew. Chem., Int. Ed.* **2007**, *46* (23), 4342−4345.

(96) Gao, J.; Ran, X.; Shi, C.; Cheng, H.; Cheng, T.; Su, Y. One-step solvothermal synthesis of highly water-soluble, negatively charged superparamagnetic Fe3O4 colloidal nanocrystal clusters. *Nanoscale* **2013**, *5* (15), 7026−7033.

(97) Liu, J.; Sun, Z.; Deng, Y.; Zou, Y.; Li, C.; Guo, X.; Xiong, L.; Gao, Y.; Li, F.; Zhao, D. Highly water-dispersible biocompatible magnetite particles with low cytotoxicity stabilized by citrate groups. *Angew. Chem., Int. Ed.* **2009**, *48* (32), 5875−5879.

(98) Luo, W.; Ma, H.; Mou, F.; Zhu, M.; Yan, J.; Guan, J. Steric-repulsion-based magnetically responsive photonic crystals. *Adv. Mater.* **2014**, *26* (7), 1058−1064.

(99) Cheng, W.; Tang, K.; Qi, Y.; Sheng, J.; Liu, Z. One-step synthesis of superparamagnetic monodisperse porous Fe3O4 hollow and core-shell spheres. *J. Mater. Chem.* **2010**, *20* (9), 1799−1805.

(100) Xuan, S.; Wang, F.; Wang, Y.-X. J.; Yu, J. C.; Leung, K. C.-F. Facile synthesis of size-controllable monodispersed ferrite nanospheres. *J. Mater. Chem.* **2010**, *20* (24), 5086−5094.

(101) Pan, L.; Peng, Z.; Yu, H.; Liang, T.; Cheng, C. Robust synthesis of highly charged superparamagnetic Fe3O4 colloidal nanocrystal clusters for magnetically responsive photonic crystals. *New J. Chem.* **2021**, *45* (36), 16511−16519.

(102) Hu, Y.; He, L.; Yin, Y. Magnetically responsive photonic nanochains. *Angew. Chem., Int. Ed.* **2011**, *123* (16), 3831−3834.

(103) Wang, M.; He, L.; Hu, Y.; Yin, Y. Magnetically rewritable photonic ink based on superparamagnetic nanochains. *J. Mater. Chem. C* **2013**, *1* (38), 6151−6156.

(104) Luo, W.; Cui, Q.; Fang, K.; Chen, K.; Ma, H.; Guan, J. Responsive Hydrogel-based Photonic Nanochains for Microenvironment Sensing and Imaging in Real Time and High Resolution. *Nano Lett.* **2020**, *20* (2), 803−811.

(105) Liu, Y.; Fan, Q.; Zhu, G.; Shi, G.; Ma, H.; Li, W.; Wu, T.; Chen, J.; Yin, Y.; Guan, J. A dual responsive photonic liquid for independent modulation of color brightness and hue. *Mater. Horiz.* **2021**, *8* (7), 2032−2040.

(106) Li, Z.; Fan, Q.; Wu, C.; Li, Y.; Cheng, C.; Yin, Y. Magnetically Tunable Plasmon Coupling of Au Nanoshells Enabled by Space-Free Confined Growth. *Nano Lett.* **2020**, *20* (11), 8242−8249.

(107) Xue, X.; Furlani, E. P. Analysis of the Dynamics of Magnetic Core−Shell Nanoparticles and Self-Assembly of Crystalline Superstructures in Gradient Fields. *J. Phys. Chem. C* **2015**, *119* (10), 5714−5726.

(108) Wu, L.; Mendoza-Garcia, A.; Li, Q.; Sun, S. Organic Phase Syntheses of Magnetic Nanoparticles and Their Applications. *Chem. Rev.* **2016**, *116* (18), 10473−10512.

(109) Tierno, P. Recent advances in anisotropic magnetic colloids: realization, assembly and applications. *Phys. Chem. Chem. Phys.* **2014**, *16* (43), 23515−23528.

(110) Ma, Z.; Mohapatra, J.; Wei, K.; Liu, J. P.; Sun, S. Magnetic Nanoparticles: Synthesis, Anisotropy, and Applications. *Chem. Rev.* **2023**, *123* (7), 3904−3943.

(111) Jun, Y. W.; Choi, J. S.; Cheon, J. Heterostructured magnetic nanoparticles: their versatility and high performance capabilities. *Chem. Commun. (Camb)* **2007**, No. 12, 1203−1214.

(112) Lu, A. H.; Salabas, E. L.; Schuth, F. Magnetic nanoparticles: synthesis, protection, functionalization, and application. *Angew. Chem., Int. Ed.* **2007**, *46* (8), 1222−1244.

(113) Bean, C. P.; Livingston, J. D. Superparamagnetism. *J. Appl. Phys.* **1959**, *30* (4), S120−S129.

(114) Wang, J.; Peng, Z.; Huang, Y.; Chen, Q. Growth of magnetite nanorods along its easy-magnetization axis of [110]. *J. Cryst. Growth* **2004**, *263* (1−4), 616−619.

(115) Kim, C. H.; Chun, H. J.; Kim, D. S.; Kim, S. Y.; Park, J.; Moon, J. Y.; Lee, G.; Yoon, J.; Jo, Y.; Jung, M.-H.; Jung, S. I.; Lee, C. J. Magnetic anisotropy of vertically aligned α-Fe2O3 nanowire array. *Appl. Phys. Lett.* **2006**, *89* (22), 223103.

(116) Kim, S. H.; Park, J. G.; Choi, T. M.; Manoharan, V. N.; Weitz, D. A. Osmotic-pressure-controlled concentration of colloidal particles in thin-shelled capsules. *Nat. Commun.* **2014**, *5*, 3068.

(117) Choi, T. M.; Park, J.-G.; Kim, Y.-S.; Manoharan, V. N.; Kim, S.-H. Osmotic-Pressure-Mediated Control of Structural Colors of Photonic Capsules. *Chem. Mater.* **2015**, *27* (3), 1014−1020.

(118) Shang, L.; Shangguan, F.; Cheng, Y.; Lu, J.; Xie, Z.; Zhao, Y.; Gu, Z. Microfluidic generation of magnetoresponsive Janus photonic crystal particles. *Nanoscale* **2013**, *5* (20), 9553−9557.

(119) Zhao, Y.; Shang, L.; Cheng, Y.; Gu, Z. Spherical colloidal photonic crystals. *Acc. Chem. Res.* **2014**, *47* (12), 3632−3642.

(120) Liu, J.; Xiao, M.; Li, C.; Li, H.; Wu, Z.; Zhu, Q.; Tang, R.; Xu, A. B.; He, L. Rugby-ball-like photonic crystal supraparticles with non-close-packed structures and multiple magneto-optical responses. *J. Mater. Chem. C* **2019**, *7* (47), 15042−15048.

(121) Dumestre, F.; Chaudret, B.; Amiens, C.; Renaud, P.; Fejes, P. Superlattices of iron nanocubes synthesized from Fe [N (SiMe3) 2] 2. *Science* **2004**, *303* (5659), 821−823.

(122) Rossi, L. *Colloidal superballs*; University Utrecht: 2012.

(123) Wang, S.-B.; Min, Y.-L.; Yu, S.-H. Synthesis and magnetic properties of uniform hematite nanocubes. *J. Phys. Chem. C* **2007**, *111* (9), 3551−3554.

(124) Sun, S.; Zeng, H.; Robinson, D. B.; Raoux, S.; Rice, P. M.; Wang, S. X.; Li, G. Monodisperse MFe2O4 (M = Fe, Co, Mn) Nanoparticles. *J. Am. Chem. Soc.* **2004**, *126* (1), 273−279.

(125) Zeng, H.; Rice, P. M.; Wang, S. X.; Sun, S. Shape-Controlled Synthesis and Shape-Induced Texture of MnFe2O4 Nanoparticles. *J. Am. Chem. Soc.* **2004**, *126* (37), 11458−11459.

(126) Xu, Y.; Sherwood, J.; Qin, Y.; Holler, R. A.; Bao, Y. A general approach to the synthesis and detailed characterization of magnetic ferrite nanocubes. *Nanoscale* **2015**, *7* (29), 12641−12649.

(127) Yang, W.; Yu, Y.; Wang, L.; Yang, C.; Li, H. Controlled synthesis and assembly into anisotropic arrays of magnetic cobalt-substituted magnetite nanocubes. *Nanoscale* **2015**, *7* (7), 2877−2882.

(128) Hakonsen, V.; Singh, G.; De Toro, J. A.; Normile, P. S.; Wahlstrom, E.; He, J.; Zhang, Z. Reconfigurable Mechanical Anisotropy in Self-Assembled Magnetic Superstructures. *Adv. Sci. (Weinh)* **2021**, *8* (8), 2002683.

(129) Roca, A. G.; Gutierrez, L.; Gavilan, H.; Fortes Brollo, M. E.; Veintemillas-Verdaguer, S.; Morales, M. D. P. Design strategies for shape-controlled magnetic iron oxide nanoparticles. *Adv. Drug. Delivery Rev.* **2019**, *138*, 68−104.

(130) Cao, Y.; Lei, X.; Chen, Q.; Kang, C.; Li, W.; Liu, B. Enhanced photocatalytic degradation of tetracycline hydrochloride by novel porous hollow cube ZnFe2O4. *J. Photochem. Photobiol., A* **2018**, *364*, 794−800.

(131) Li, B.; Chen, J.; Han, L.; Bai, Y.; Fan, Q.; Wu, C.; Wang, X.; Lee, M.; Xin, H. L.; Han, Z.; Yin, Y. Ligand-Assisted Solid-State Transformation of Nanoparticles. *Chem. Mater.* **2020**, *32* (7), 3271−3277.

(132) Rossi, L.; Donaldson, J. G.; Meijer, J. M.; Petukhov, A. V.; Kleckner, D.; Kantorovich, S. S.; Irvine, W. T. M.; Philipse, A. P.; Sacanna, S. Self-organization in dipolar cube fluids constrained by competing anisotropies. *Soft Matter* **2018**, *14* (7), 1080−1087.

(133) Lee, S. H.; Liddell, C. M. Anisotropic magnetic colloids: a strategy to form complex structures using nonspherical building blocks. *Small* **2009**, *5* (17), 1957−1962.

(134) Ahniyaz, A.; Sakamoto, Y.; Bergström, L. Magnetic field-induced assembly of oriented superlattices from maghemite nanocubes. *Proc. Natl. Acad. Sci. U.S.A.* **2007**, *104* (45), 17570−17574.

(135) Disch, S.; Wetterskog, E.; Hermann, R. P.; Salazar-Alvarez, G.; Busch, P.; Bruckel, T.; Bergstrom, L.; Kamali, S. Shape induced symmetry in self-assembled mesocrystals of iron oxide nanocubes. *Nano Lett.* **2011**, *11* (4), 1651−1656.

(136) Singh, G.; Chan, H.; Baskin, A.; Gelman, E.; Repnin, N.; Král, P.; Klajn, R. Self-assembly of magnetite nanocubes into helical superstructures. *Science* **2014**, *345* (6201), 1149−1153.

(137) Aoshima, M.; Ozaki, M.; Satoh, A. Structural Analysis of Self-Assembled Lattice Structures Composed of Cubic Hematite Particles. *J. Phys. Chem. C* **2012**, *116* (33), 17862−17871.

(138) Yang, Y.; Liu, X.; Lv, Y.; Herng, T. S.; Xu, X.; Xia, W.; Zhang, T.; Fang, J.; Xiao, W.; Ding, J. Orientation Mediated Enhancement on Magnetic Hyperthermia of Fe3O4Nanodisc. *Adv. Funct. Mater.* **2015**, *25* (5), 812−820.

(139) Gao, Y.; Bao, Y.; Pakhomov, A. B.; Shindo, D.; Krishnan, K. M. Spiral spin order of self-assembled Co nanodisk arrays. *Phys. Rev. Lett.* **2006**, *96* (13), 137205.

(140) Shuai, M.; Klittnick, A.; Shen, Y.; Smith, G. P.; Tuchband, M. R.; Zhu, C.; Petschek, R. G.; Mertelj, A.; Lisjak, D.; Copic, M.; Maclennan, J. E.; Glaser, M. A.; Clark, N. A. Spontaneous liquid

crystal and ferromagnetic ordering of colloidal magnetic nanoplates. *Nat. Commun.* **2016**, *7*, 10394.

(141) Ferk, G.; Krajnc, P.; Hamler, A.; Mertelj, A.; Cebollada, F.; Drofenik, M.; Lisjak, D. Monolithic Magneto-Optical Nanocomposites of Barium Hexaferrite Platelets in PMMA. *Sci. Rep.* **2015**, *5*, 11395.

(142) Coughlan, A. C. H.; Bevan, M. A. Effective colloidal interactions in rotating magnetic fields. *J. Chem. Phys.* **2017**, *147* (7), 074903.

(143) Zhang, T.; Peng, X.; Li, J.; Yang, Y.; Xu, J.; Wang, P.; Jin, D.; Jin, H.; Hong, B.; Wang, X.; Ge, H. Structural, magnetic and electromagnetic properties of SrFe12O19 ferrite with particles aligned in a magnetic field. *J. Alloys Compd.* **2017**, *690*, 936−941.

(144) Zhang, C.; Wu, Z.; Chen, Z.; Pan, L.; Li, J.; Xiao, M.; Wang, L.; Li, H.; Huang, Z.; Xu, A.-B.; Li, C.; He, L. Photonic nanostructures of nanodiscs with multiple magneto-optical properties. *J. Mater. Chem. C* **2020**, *8* (45), 16067−16072.

(145) Sugimoto, T.; Khan, M. M.; Muramatsu, A. Preparation of monodisperse peanut-type α-Fe2O3 particles from condensed ferric hydroxide gel. *Colloids Surf. A Physicochem. Eng. Asp.* **1993**, *70* (2), 167−169.

(146) Lee, S. H.; Song, Y.; Hosein, I. D.; Liddell, C. M. Magnetically responsive and hollow colloids from nonspherical core−shell particles of peanut-like shape. *J. Mater. Chem.* **2009**, *19* (3), 350−355.

(147) Ge, J.; Hu, Y.; Zhang, T.; Yin, Y. Superparamagnetic composite colloids with anisotropic structures. *J. Am. Chem. Soc.* **2007**, *129* (29), 8974−8975.

(148) Zhao, B.; Zhou, H.; Liu, C.; Long, Y.; Yang, G.; Tung, C.-H.; Song, K. Fabrication and directed assembly of magnetic Janus rods. *New J. Chem.* **2016**, *40* (8), 6541−6545.

(149) Li, S.; Wang, L.; Liu, B. Fabrication of magnetic colloidal bicones and their switchable self-assembly. *Soft Matter* **2020**, *16* (34), 8024−8032.

(150) Sacanna, S.; Rossi, L.; Pine, D. J. Magnetic click colloidal assembly. *J. Am. Chem. Soc.* **2012**, *134* (14), 6112−6115.

(151) Jia, Z.; Kim, J. H.; Yi, G. R.; Lee, S. S. Transition of Dielectrophoresis-Assembled 2D Crystals to Interlocking Structures under a Magnetic Field. *Langmuir* **2018**, *34* (41), 12412−12418.

(152) Kim, J. H.; Hwang, H. J.; Oh, J. S.; Sacanna, S.; Yi, G. R. Monodisperse Magnetic Silica Hexapods. *J. Am. Chem. Soc.* **2018**, *140* (29), 9230−9235.

(153) Cai, Z.; Li, Z.; Ravaine, S.; He, M.; Song, Y.; Yin, Y.; Zheng, H.; Teng, J.; Zhang, A. From colloidal particles to photonic crystals: advances in self-assembly and their emerging applications. *Chem. Soc. Rev.* **2021**, *50* (10), 5898−5951.

(154) Yablonovitch, E. Photonic Crystals. *J. Mod. Opt.* **1994**, *41* (2), 173−194.

(155) Maruo, S.; Fourkas, J. T. Recent progress in multiphoton microfabrication. *Laser & Photonics Review* **2008**, *2* (1−2), 100−111.

(156) Olsson, R. H., Iii; El-Kady, I. Microfabricated phononic crystal devices and applications. *Meas. Sci. Technol.* **2009**, *20* (1), 012002.

(157) von Freymann, G.; Kitaev, V.; Lotsch, B. V.; Ozin, G. A. Bottom-up assembly of photonic crystals. *Chem. Soc. Rev.* **2013**, *42* (7), 2528−2554.

(158) Fan, Q.; Li, Z.; Yin, Y. Magnetic assembly of colloidal nanoparticles into responsive photonic crystals. In *Encyclopedia of Nanomaterials*; Yin, Y.; Lu, Y.; Xia, Y., Eds.; Elsevier: Oxford, 2023; Vol. 3, pp 65−78.

(159) Ge, J.; Hu, Y.; Yin, Y. Highly Tunable Superparamagnetic Colloidal Photonic Crystals. *Angew. Chem., Int. Ed.* **2007**, *119* (39), 7572−7575.

(160) Luo, W.; Yan, J.; Tan, Y.; Ma, H.; Guan, J. Rotating 1-D magnetic photonic crystal balls with a tunable lattice constant. *Nanoscale* **2017**, *9* (27), 9548−9555.

(161) Ge, J.; Lee, H.; He, L.; Kim, J.; Lu, Z.; Kim, H.; Goebl, J.; Kwon, S.; Yin, Y. Magnetochromatic Microspheres: Rotating Photonic Crystals. *J. Am. Chem. Soc.* **2009**, *131* (43), 15687−15694.

(162) Kim, H.; Ge, J.; Kim, J.; Choi, S.-e.; Lee, H.; Lee, H.; Park, W.; Yin, Y.; Kwon, S. Structural colour printing using a magnetically

tunable and lithographically fixable photonic crystal. *Nat. Photonics* **2009**, *3* (9), 534−540.

(163) Wang, W.; Fan, X.; Li, F.; Qiu, J.; Umair, M. M.; Ren, W.; Ju, B.; Zhang, S.; Tang, B. Magnetochromic photonic hydrogel for an alternating magnetic field-responsive color display. *Adv. Opt. Mater.* **2018**, *6* (4), 1701093.

(164) Cai, J.; Luo, W.; Pan, J.; Li, G.; Pu, Y.; Si, L.; Shi, G.; Shao, Y.; Ma, H.; Guan, J. Glucose-Sensing Photonic Nanochain Probes with Color Change in Seconds. *Adv. Sci. (Weinh)* **2022**, *9* (9), No. e2105239.

(165) Hu, H.; Chen, Q.-W.; Tang, J.; Hu, X.-Y.; Zhou, X.-H. Photonic anti-counterfeiting using structural colors derived from magnetic-responsive photonic crystals with double photonic bandgap heterostructures. *J. Mater. Chem.* **2012**, *22* (22), 11048−11053.

(166) Li, G.; Luo, W.; Che, Z.; Pu, Y.; Deng, P.; Shi, L.; Ma, H.; Guan, J. Lipophilic Magnetic Photonic Nanochains for Practical Anticounterfeiting. *Small* **2022**, *18* (21), No. e2200662.

(167) Hu, H.; Zhong, H.; Chen, C.; Chen, Q. Magnetically responsive photonic watermarks on banknotes. *J. Mater. Chem. C* **2014**, *2* (19), 3695−3702.

(168) Ge, J.; Goebl, J.; He, L.; Lu, Z.; Yin, Y. Rewritable Photonic Paper with Hygroscopic Salt Solution as Ink. *Adv. Mater.* **2009**, *21* (42), 4259−4264.

(169) Qiu, M.; He, S. Large complete band gap in two-dimensional photonic crystals with elliptic air holes. *Phys. Rev. B* **1999**, *60* (15), 10610.

(170) Li, Z.-Y.; Wang, J.; Gu, B.-Y. Creation of partial band gaps in anisotropic photonic-band-gap structures. *Phys. Rev. B* **1998**, *58* (7), 3721.

(171) Li, Z.; Wang, X.; Han, L.; Zhu, C.; Xin, H.; Yin, Y. Multicolor Photonic Pigments for Rotation-Asymmetric Mechanochromic Devices. *Adv. Mater.* **2022**, *34* (4), No. e2107398.

(172) Schadt, M. Liquid crystal materials and liquid crystal displays. *Annu. Rev. Mater. Sci.* **1997**, *27* (1), 305−379.

(173) Li, Z.; Yin, Y. Stimuli-Responsive Optical Nanomaterials. *Adv. Mater.* **2019**, *31* (15), No. e1807061.

(174) Binnemans, K.; Galyametdinov, Y. G.; Van Deun, R.; Bruce, D. W.; Collinson, S. R.; Polishchuk, A. P.; Bikchantaev, I.; Haase, W.; Prosvirin, A. V.; Tinchurina, L.; et al. Rare-earth-containing magnetic liquid crystals. *J. Am. Chem. Soc.* **2000**, *122* (18), 4335−4344.

(175) Binnemans, K.; Bruce, D. W.; Collinson, S. R.; Deun, R. V.; Galyametdinov, Y. G.; Martin, F. Towards magnetic liquid crystals. *Philos. Trans. Royal Soc. A* **1999**, *357* (1762), 3063−3077.

(176) Wang, M.; He, L.; Zorba, S.; Yin, Y. Magnetically actuated liquid crystals. *Nano Lett.* **2014**, *14* (7), 3966−3971.

(177) Cui, J.; Kramer, M.; Zhou, L.; Liu, F.; Gabay, A.; Hadjipanayis, G.; Balasubramanian, B.; Sellmyer, D. Current progress and future challenges in rare-earth-free permanent magnets. *Acta Mater.* **2018**, *158*, 118−137.

(178) Coey, J. Permanent magnetism. *Solid State Commun.* **1997**, *102* (2−3), 101−105.

(179) Sellmyer, D. J. Strong magnets by self-assembly. *Nature* **2002**, *420* (6914), 374−375.

(180) Buschow, K. Intermetallic compounds of rare-earth and 3d transition metals. *Rep. Prog. Phys.* **1977**, *40* (10), 1179.

(181) Chu, S. *Critical materials strategy*; DIANE Publishing: 2011.

(182) Li, D.; Pan, D.; Li, S.; Zhang, Z. Recent developments of rare-earth-free hard-magnetic materials. *Sci. China: Phys. Mech. Astron.* **2016**, *59* (1), 1−17.

(183) Soumare, Y.; Piquemal, J. Y.; Maurer, T.; Ott, F.; Chaboussant, G.; Falqui, A.; Viau, G. Oriented magnetic nanowires with high coercivity. *J. Mater. Chem.* **2008**, *18* (46), 5696−5702.

(184) Ott, F.; Maurer, T.; Chaboussant, G.; Soumare, Y.; Piquemal, J. Y.; Viau, G. Effects of the shape of elongated magnetic particles on the coercive field. *J. Appl. Phys.* **2009**, *105* (1), 013915.

(185) Ramazani, A.; Almasi Kashi, M.; Montazer, A. H. Fabrication of single crystalline, uniaxial single domain Co nanowire arrays with high coercivity. *J. Appl. Phys.* **2014**, *115* (11), 113902.

(186) Viau, G.; García, C.; Maurer, T.; Chaboussant, G.; Ott, F.; Soumare, Y.; Piquemal, J. Y. Highly crystalline cobalt nanowires with high coercivity prepared by soft chemistry. *Phys. Status Solidi* **2009**, *206* (4), 663−666.

(187) Mohapatra, J.; Xing, M.; Elkins, J.; Beatty, J.; Liu, J. P. Extraordinary Magnetic Hardening in Nanowire Assemblies: the Geometry and Proximity Effects. *Adv. Funct. Mater.* **2021**, *31* (13), 2010157.

(188) Gandha, K.; Elkins, K.; Poudyal, N.; Liu, X.; Liu, J. P. High energy product developed from cobalt nanowires. *Sci. Rep.* **2014**, *4* (1), 5345.

(189) Anagnostopoulou, E.; Grindi, B.; Lacroix, L. M.; Ott, F.; Panagiotopoulos, I.; Viau, G. Dense arrays of cobalt nanorods as rare-earth free permanent magnets. *Nanoscale* **2016**, *8* (7), 4020−4029.

(190) Ener, S.; Anagnostopoulou, E.; Dirba, I.; Lacroix, L.-M.; Ott, F.; Blon, T.; Piquemal, J.-Y.; Skokov, K. P.; Gutfleisch, O.; Viau, G. Consolidation of cobalt nanorods: A new route for rare-earth free nanostructured permanent magnets. *Acta Mater.* **2018**, *145*, 290−297.

(191) Ait Atmane, K.; Zighem, F.; Soumare, Y.; Ibrahim, M.; Boubekri, R.; Maurer, T.; Margueritat, J.; Piquemal, J.-Y.; Ott, F.; Chaboussant, G.; Schoenstein, F.; Jouini, N.; Viau, G. High temperature structural and magnetic properties of cobalt nanorods. *J. Solid State Chem.* **2013**, *197*, 297−303.

(192) Bergstrom, L.; Sturm nee Rosseeva, E. V.; Salazar-Alvarez, G.; Colfen, H. Mesocrystals in Biominerals and Colloidal Arrays. *Acc. Chem. Res.* **2015**, *48* (5), 1391−1402.

(193) Currey, J. D. Mechanical properties of mother of pearl in tension. *Proc. R. Soc. London Ser. B. Biol. Sci.* **1977**, *196* (1125), 443−463.

(194) Shevchenko, E. V.; Talapin, D. V.; Kotov, N. A.; O'Brien, S.; Murray, C. B. Structural diversity in binary nanoparticle superlattices. *Nature* **2006**, *439* (7072), 55−59.

(195) Dong, A.; Chen, J.; Vora, P. M.; Kikkawa, J. M.; Murray, C. B. Binary nanocrystal superlattice membranes self-assembled at the liquid-air interface. *Nature* **2010**, *466* (7305), 474−477.

(196) Redl, F. X.; Cho, K.-S.; Murray, C. B.; O'Brien, S. Three-dimensional binary superlattices of magnetic nanocrystals and semiconductor quantum dots. *Nature* **2003**, *423* (6943), 968−971.

(197) Paik, T.; Diroll, B. T.; Kagan, C. R.; Murray, C. B. Binary and ternary superlattices self-assembled from colloidal nanodisks and nanorods. *J. Am. Chem. Soc.* **2015**, *137* (20), 6662−6669.

(198) Quan, Z.; Fang, J. Superlattices with non-spherical building blocks. *Nano Today* **2010**, *5* (5), 390−411.

(199) Chen, H.; Sulejmanovic, D.; Moore, T.; Colvin, D. C.; Qi, B.; Mefford, O. T.; Gore, J. C.; Alexis, F.; Hwu, S. J.; Anker, J. N. Iron-Loaded Magnetic Nanocapsules for pH-Triggered Drug Release and MRI Imaging. *Chem. Mater.* **2014**, *26* (6), 2105−2112.

(200) Zhao, P.; Liu, S.; Koriath, A. T.; Gao, X. Partial Magneto-Endosomalysis for Cytosolic Delivery of Antibodies. *Bioconjugate Chem.* **2022**, *33* (2), 363−368.

(201) Yang, P.; Quan, Z.; Hou, Z.; Li, C.; Kang, X.; Cheng, Z.; Lin, J. A magnetic, luminescent and mesoporous core-shell structured composite material as drug carrier. *Biomaterials* **2009**, *30* (27), 4786−4795.

(202) Serantes, D.; Simeonidis, K.; Angelakeris, M.; Chubykalo-Fesenko, O.; Marciello, M.; Morales, M. d. P.; Baldomir, D.; Martinez-Boubeta, C. Multiplying Magnetic Hyperthermia Response by Nanoparticle Assembling. *J. Phys. Chem. C* **2014**, *118* (11), 5927−5934.

(203) Mamiya, H.; Fukumoto, H.; Cuya Huaman, J. L.; Suzuki, K.; Miyamura, H.; Balachandran, J. Estimation of Magnetic Anisotropy of Individual Magnetite Nanoparticles for Magnetic Hyperthermia. *ACS Nano* **2020**, *14* (7), 8421−8432.

(204) Abenojar, E. C.; Wickramasinghe, S.; Bas-Concepcion, J.; Samia, A. C. S. Structural effects on the magnetic hyperthermia properties of iron oxide nanoparticles. *Prog. Nat. Sci.: Mater. Int.* **2016**, *26* (5), 440−448.

(205) Laurent, S.; Dutz, S.; Hafeli, U. O.; Mahmoudi, M. Magnetic fluid hyperthermia: focus on superparamagnetic iron oxide nanoparticles. *Adv. Colloid Interface Sci.* **2011**, *166* (1−2), 8−23.

(206) Corr, S. A.; Byrne, S. J.; Tekoriute, R.; Meledandri, C. J.; Brougham, D. F.; Lynch, M.; Kerskens, C.; O'Dwyer, L.; Gun'ko, Y. K. Linear assemblies of magnetic nanoparticles as MRI contrast agents. *J. Am. Chem. Soc.* **2008**, *130* (13), 4214−4215.

(207) Lee, N.; Hyeon, T. Designed synthesis of uniformly sized iron oxide nanoparticles for efficient magnetic resonance imaging contrast agents. *Chem. Soc. Rev.* **2012**, *41* (7), 2575−2589.

(208) Li, L.; Jiang, W.; Luo, K.; Song, H.; Lan, F.; Wu, Y.; Gu, Z. Superparamagnetic iron oxide nanoparticles as MRI contrast agents for non-invasive stem cell labeling and tracking. *Theranostics* **2013**, *3* (8), 595−615.

(209) Gavilan, H.; Simeonidis, K.; Myrovali, E.; Mazario, E.; Chubykalo-Fesenko, O.; Chantrell, R.; Balcells, L.; Angelakeris, M.; Morales, M. P.; Serantes, D. How size, shape and assembly of magnetic nanoparticles give rise to different hyperthermia scenarios. *Nanoscale* **2021**, *13* (37), 15631−15646.

(210) Hu, K.; Sun, J.; Guo, Z.; Wang, P.; Chen, Q.; Ma, M.; Gu, N. A novel magnetic hydrogel with aligned magnetic colloidal assemblies showing controllable enhancement of magnetothermal effect in the presence of alternating magnetic field. *Adv. Mater.* **2015**, *27* (15), 2507−2514.

(211) Bai, Y.; Gao, C.; Yin, Y. Fully alloyed Ag/Au nanorods with tunable surface plasmon resonance and high chemical stability. *Nanoscale* **2017**, *9* (39), 14875−14880.

(212) Zeng, J.; Zhang, Y.; Zeng, T.; Aleisa, R.; Qiu, Z.; Chen, Y.; Huang, J.; Wang, D.; Yan, Z.; Yin, Y. Anisotropic plasmonic nanostructures for colorimetric sensing. *Nano Today* **2020**, *32*, 100855.

(213) Li, Z.; Myung, N. V.; Yin, Y. Light-powered soft steam engines for self-adaptive oscillation and biomimetic swimming. *Science Robotics* **2021**, *6* (61), No. eabi4523.

(214) Cobley, C. M.; Skrabalak, S. E.; Campbell, D. J.; Xia, Y. Shape-Controlled Synthesis of Silver Nanoparticles for Plasmonic and Sensing Applications. *Plasmonics* **2009**, *4* (2), 171−179.

(215) Zheng, J.; Cheng, X.; Zhang, H.; Bai, X.; Ai, R.; Shao, L.; Wang, J. Gold Nanorods: The Most Versatile Plasmonic Nanoparticles. *Chem. Rev.* **2021**, *121* (21), 13342−13453.

(216) Ringe, E. Shapes, Plasmonic Properties, and Reactivity of Magnesium Nanoparticles. *J. Phys. Chem. C Nanomater. Interfaces* **2020**, *124* (29), 15665−15679.

(217) He, H.; Liu, J.; Li, K.; Yin, Z.; Wang, J.; Luo, D.; Liu, Y. J. Linearly Polarized Emission from Shear-Induced Nematic Phase Upconversion Nanorods. *Nano Lett.* **2020**, *20* (6), 4204−4210.

(218) Artemyev, M.; Möller, B.; Woggon, U. Unidirectional alignment of CdSe nanorods. *Nano Lett.* **2003**, *3* (4), 509−512.

(219) Zhang, C.; Chen, J.; Wang, S.; Kong, L.; Lewis, S. W.; Yang, X.; Rogach, A. L.; Jia, G. Metal Halide Perovskite Nanorods: Shape Matters. *Adv. Mater.* **2020**, *32* (46), No. e2002736.

(220) Grzelczak, M.; Rodríguez-González, B.; Pérez-Juste, J.; Liz-Marzán, L. M. Quasi-Epitaxial Growth of Ni Nanoshells on Au Nanorods. *Adv. Mater.* **2007**, *19* (17), 2262−2266.

(221) Rizvi, M. H.; Wang, R.; Schubert, J.; Crumpler, W. D.; Rossner, C.; Oldenburg, A. L.; Fery, A.; Tracy, J. B. Magnetic Alignment for Plasmonic Control of Gold Nanorods Coated with Iron Oxide Nanoparticles. *Adv. Mater.* **2022**, *34* (40), No. e2203366.

(222) Li, Z.; Jin, J.; Yang, F.; Song, N.; Yin, Y. Coupling magnetic and plasmonic anisotropy in hybrid nanorods for mechanochromic responses. *Nat. Commun.* **2020**, *11* (1), 2883.

(223) Jung, I.; Ih, S.; Yoo, H.; Hong, S.; Park, S. Fourier Transform Surface Plasmon Resonance of Nanodisks Embedded in Magnetic Nanorods. *Nano Lett.* **2018**, *18* (3), 1984−1992.

(224) Yan, J.; Bae, S. C.; Granick, S. Colloidal superstructures programmed into magnetic Janus particles. *Adv. Mater.* **2015**, *27* (5), 874−879.

(225) Yan, J.; Bloom, M.; Bae, S. C.; Luijten, E.; Granick, S. Linking synchronization to self-assembly using magnetic Janus colloids. *Nature* **2012**, *491* (7425), 578−581.

(226) Martin, J. E.; Snezhko, A. Driving self-assembly and emergent dynamics in colloidal suspensions by time-dependent magnetic fields. *Rep. Prog. Phys.* **2013**, *76* (12), 126601.